PH700 Research Project Report 2012/13

Investigations of hypervelocity impact flashes using commercially available recording equipment.

Tilo Hohenschläger / Student No.: 07437100

th202@kent.ac.uk

MPhys – Astronomy, Space Science and Astrophysics

Supervisor: Dr Mark Price

University of Kent

School of Physical Sciences

Table of Content

Appendix

Abstract

An observational program of hypervelocity impacts was run for collecting impact flashes and spectra data. These impacts varied in speed and target/impactor compositions. To achieve this, two newly procured digital single-lens reflex (DSLR) cameras (a Nikon D3200 and Nikon 1 V1) were characterised. By photographing a helium emission spectrum a linear relation was found as expected for the dependence of the wavelength and distance. Through this, the equation of a straight line of $\lambda = 2.4704\ d + 454.63$ nm was obtained. Further calibration work carried out for these two cameras produced a 27 % error in the average pixel value compared to the RAW data for the red pixels, a 36 % error in the pixel value compared to the RAW data for the green pixels, and a 12 % error compared to the RAW data for the blue pixels for the Nikon 1 V1. The errors calculated for the average pixel value of the Nikon D3200 for the red, green and blue pixels were 16.4%, 42.7%, and -2.7% respectively. After eliminating the current obstacle of the image saturation, a database of impact images and spectra, freely accessible for use by the shock physics and hypervelocity impact research communities, will be created.

Introduction

The launch of the first artificial satellite in 1957 marked the beginning of the "space age". This new era provided the technology for new and useful methods for the study of the space environment. Launching spacecraft into orbit exposes the vehicle to a harsh environment, including the serious hazard of damage from meteoritic bombardment. For this reason it was necessary to develop suitable measurement techniques and to understand more fully the phenomena associated with the impact of high-velocity meteoroids on surfaces [1]. One of the phenomena associated with a hypervelocity impact is the generation of an intense, short-lived, flash of light – the "impact flash".

To study these various aspects of high-speed impact phenomena, the two-stage light gas gun of the Hypervelocity Impact Facility of the University of Kent at Canterbury was utilized for this project. This projects aims are to measure the colour temperature of the impact flash in order to calculate the speed of impact (assuming that greater kinetic energy leads to shorter wavelength light emission) and to measure the impact flash intensity in order to calculate the impactor size. Measuring light flashes in hypervelocity impacts has been investigated for several decades. Eichhorn observed the light flash in hypervelocity impacts of micron-sized particles on metals using a Van de Graaff facility instead of a two-stage light gas gun [2, 3, and 4]. Burchell et al. investigated light flashes from hypervelocity impacts on ice [5]. Recently, however, there has been a renewed interest in the subject, at the European Planetary Science Congress (EPSC) in 2012, Madiedo et al. [6] and Margonis et al. [7] presented their preliminary results of their observational programmes of the lunar surface detecting impact flashes. Both teams were using telescopes with high-sensitivity

CCD video and image capturing capabilities to monitor the night side of the Moon. Monitoring programs like that provide the quantitative and qualitative measurements of the meteor population near Earth and can be used for hazard mitigation purposes in future space exploration as outlined by the National Aeronautics and Space Administration (NASA) in their report “Voyages: Charting the Course for Sustainable Human Space Exploration.”[8]. The results from this project can be utilized as a starting point for anyone who is interested to set up their own monitoring programme (well within the budget of an amateur astronomy society) as well as a source for calibration data for national space agencies like NASA, the European Space Agency (ESA) or the Japanese Aerospace Exploration Agency (JAXA) etc.

Shockwaves and Impacts

When solid substances are subjected to powerful releases shocks they are forced into unusual and particular conditions which result in the propagation of high pressure mechanical waves within the solid body [9]. These shock waves are defined as discontinuous in pressure, temperature and density [10]. To illustrate this, one can think of a moving shock front and considers the domain immediately ahead of and behind the shock front. Ahead of the shock front, the pressure is P_0 (GPa), the density is ρ_0 (kg/m^3), and the temperature is T_0 (K). Behind the shock front they are P, ρ, and T, respectively. While the velocity of the shock front is U_S (m s^{-1}), the particles ahead of the front are stationary. At the front and behind it, they are moving at a velocity U_P. This can be used to derive the equations for the conservation of mass, momentum, and energy. These equations are [10]:

Mass: $$\rho_0 \, U_S = \rho \, (U_S - U_P) \qquad \text{Eqn. (1)}$$

Momentum: $$P - P_0 = \rho_0 U_S U_P$$ Eqn. (2)

Energy: $$E - E_0 = \frac{1}{2}(P + P_0)(V_0 - V)$$ Eqn. (3)

To determine the parameters an additional equation has to be used, and is known as the equation of state (EOS). However the resulting linear equation is not valid for materials which undergo phase transitions during shocking. This leads to experimentally measuring the equation of state for a given material. The relation between Pressure and Density established from Equation 3 is known as a "Hugoniot curve" and is shown in Figure 1. In the case that the initial conditions are known, one can plot a series of data points for an object undergoing a series of shock waves of varying force in respect to the compression states. The Rayleigh line connects points analogous to the initial and final state on a graph of pressure. The area between the Rayleigh line and the curve corresponds to the total energy for the transformation from the initial state to the final state to occur.

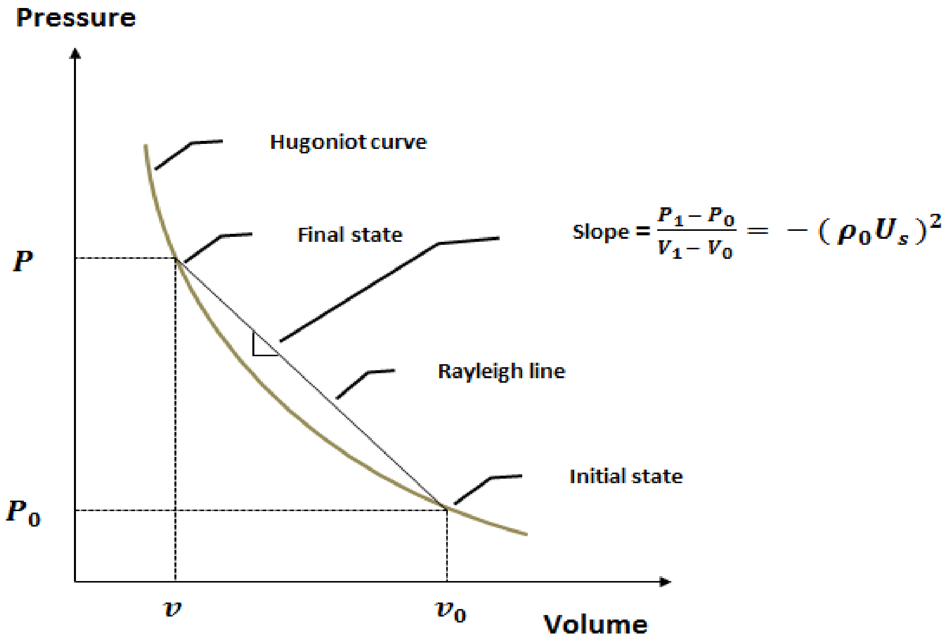

Figure 1: Schematic of a Hugoniot curve from a shock experiment showing a Rayleigh line [10].

Impact flashes in hypervelocity impacts

Hypervelocity impacts occur when the speed of impact exceeds the speed of the compression waves in both the target and in the projectile. Because the energy of the impact is delivered faster than it can be dissipate, the impact causes extreme transient densities and temperatures at the impact site [11]. This can cause melting and vapourisation of the impactor and the target material involved, and such impacts produce luminous phenomena. These so-called impact light flashes occur because of the conversion of a fraction of the projectiles kinetic energy into radiant energy [12].

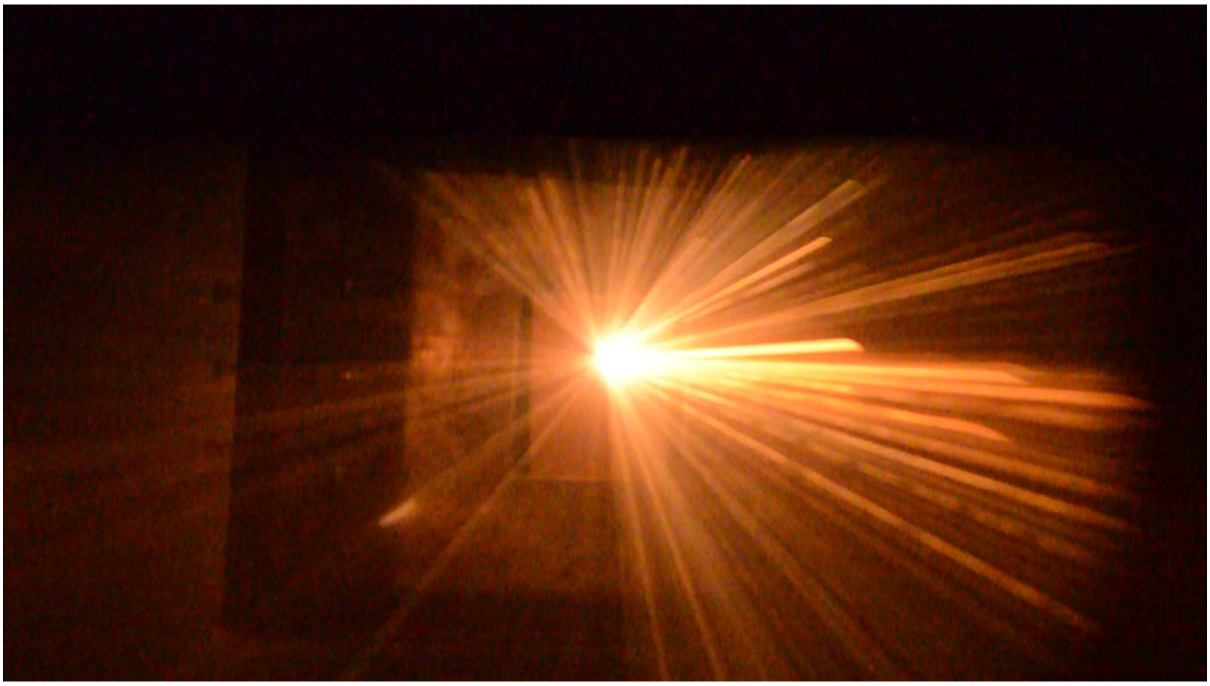

Figure 2: Impact light flash recorded for the Shot ID G051012#3

As mentioned earlier, multiple investigations into the impact light flash have been made. Friichtenicht [12] observed the light flash with photomultiplier tubes and reported in his series of experiments (which used a two MV Van de Graaff accelerator and Carbonyl iron spheres on various target materials), two possible sources of radiant energy: firstly blackbody emission from heated material and secondly other radiation from excited atoms in the plasma cloud. He also found a strong velocity dependence on the impact flash [12]. Eichhorn [2, 3] also used photomultiplier tubes to research impact flashes of iron particles. To some extent aluminium, carbon and tungsten projectiles were also used. These projectiles were accelerated to velocities between 0.5 kms^{-1} and 35 kms^{-1} via a Van de Graaff accelerator, initially impacting tungsten and gold targets. To determine the relationship between the light generation efficiency and the target material, 15 different target materials were impacted altogether. Eichhorn [3] found that the light intensity (I) and the total light energy (E in erg) are related to the mass of the projectile (m in g) and the projectiles velocity (v in km s^{-1}) in the form of $I = c_1 m v^{4.1}$ and $E = c_2 m v^{3.2}$, where c_1 and c_2 are constants depending on projectile and target material. In addition it was noticed that the light intensity was sensitive to pressure changes in the impact chamber. Below a threshold value of ≈ 10^{-3} mbar the light intensity was independent of the pressure. Above 10^{-3} mbar the light intensity increases with increasing pressure and reaches a maximum at around 0.1 mbar. This was explained by the conversion of the thermal energy of the expanding gas and plasma into light energy through residual gas collisions [3].

The passage of the shock wave and its subsequent release wave into the projectile and target releases sufficient energy to vapourise the projectile and part of the target, which causes impact ionisation in hypervelocity impacts [11]. Figure 2 shows the plasma generation and expansion process in hypervelocity impacts.

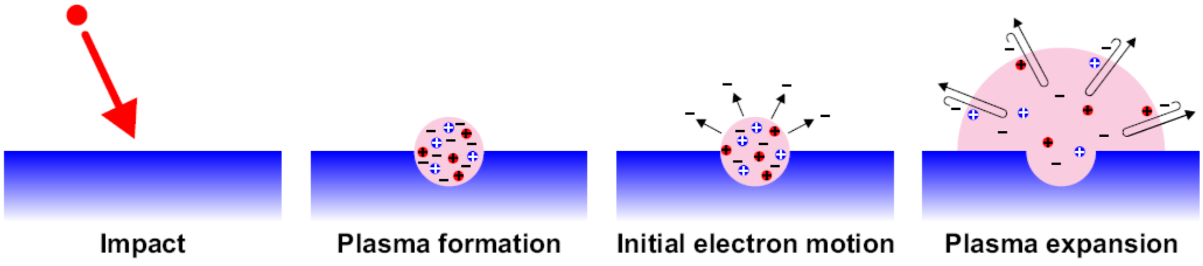

Figure 3: Depiction of the plasma generation and expansion process due to hypervelocity impacts [13].

At the outset, a particle impacts a target with hypervelocity speeds. As stated earlier, the kinetic energy of the particle is partially converted to vapourise and ionise target and projectile materials. This produces a small dense plasma formed by ionisation of material from the impactor and target. The plasma expands it quickly, and becomes collision-free by dilution. Considering their higher mobility, electrons expand outward faster than ions, hence creating an ambipolar electric field which pulls the electrons back towards the ions. Because of the slower expansion of the ions, the electrons oscillate about the ion front due to the ambipolar electric field, radiating at the plasma frequency [13].

The two-stage light gas gun

The Two-Stage Light Gas Gun (LGG) of the Hypervelocity Impact Facility at the University of Kent is used for investigations of hypervelocity impact phenomena at velocities of 1.3 – 8.5 kms^{-1}. The gun can fire single projectiles between 0.8 mm and 3.0 mm in diameter, or < 1 µm – 500 µm diameter bodies in buck-shot style firings. Through collaboration with NASA the laboratory was able to secure a new target chamber which increased the possible target diameter size from 0.2 m to 1.0 m. Figure 4 shows the gun with the new white target chamber at the far end of the gun. The LGG uses a Two-Stage system. The initial acceleration of a nylon piston is provided by burning a powder charge. The movement of

Figure 4: The LGG of the University of Kent.

this piston is used to compress a gas of low molecular mass, typically hydrogen, until it causes an aluminium burst disc to burst in the breech. The energy from the light gas by the burst is released into the next stage of the LGG, which is evacuated so that the air resistance becomes negligible. Depending on the setup of the experiment, a typical pressure in the launch tube and the range downstream of the sabot is approximately 0.1 mbar before firing. A sabot is placed in the launch tube containing the projectile and this is accelerated to hypervelocities down the launch tube. After that it enters the blast tank. Figure 5 shows a schematic diagram of the LGG. Due to the rifling of the launch tube the sabot is spinning and will separate into four pieces due to centripetal forces. These split pieces are intercepted by the stop plate which is equipped with an impact sensor. When impacted the shockwave transmitted through the stop plate produces an electrical signal, which is monitored on an oscilloscope. The projectile continues through the laser curtains, where the velocity of the projectile is measured. It then enters the Target Chamber where the target for that experiment is placed. To fire the gun, a pendulum is placed suspended at 50° from vertical. To hold it at that angle a switch mechanism is installed and controlled from a separate firing room. After releasing that pendulum, it will strike the preinstalled firing pin, igniting the primer and setting off the cartridge. For safety reasons, no personnel are present in the firing room when the gun is fired [11].

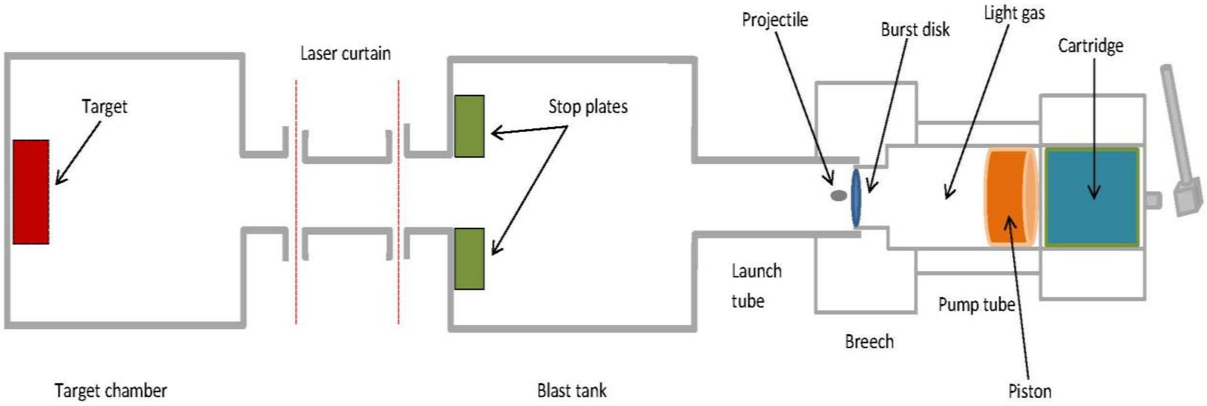

Figure 5: Schematic diagram of the Light Gas Gun.

Method

This project aims were designed to be two fold. The main aim was to collect data from hypervelocity impact flashes to create a spectra and impact image database for the scientific community, which can be used for calibration purposes, and secondly as a repeatable exercise and with budgetary constraints in mind, to encourage amateur astronomer members of the public to set up their own monitoring programmes. With this reasoning the decision was made to procure two midrange consumers digital single-lens reflex (DSLR) cameras, a Nikon D3200 and Nikon 1 V1. Figure 6 and 7 show the two models in their standard configuration.

Figure 6: Nikon D3200

Figure 7: Nikon 1 V1

These types of cameras employ Charge Coupled Devices (CCDs) for image recording. To obtain a colour image, RGB filters are mounted in front of the CCD. These filters are known as Bayer filters. The RGB signals are then co-added to get a true colour image. Figure 8 shows a filter arrangement and a cross-section of a sensor. To note in Figure 9, is the fact that there are twice as many green as red/blue pixels to mimic the eye's sensitivity to green light.

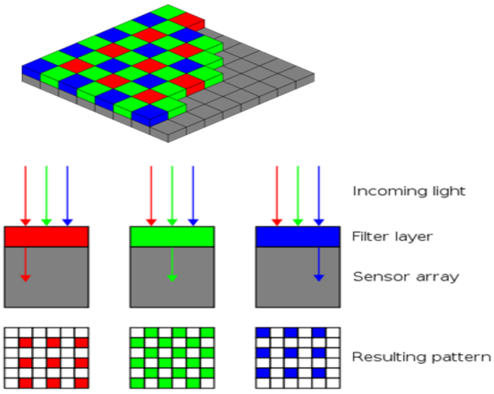

Figure 8: Bayer colour filter arrangement and profile/cross-section of sensor [14]

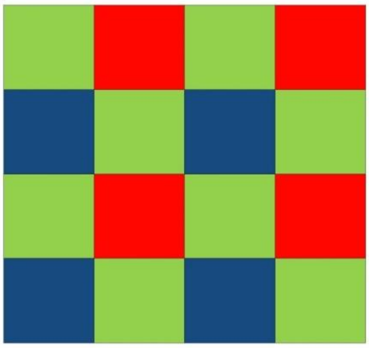

Figure 9:The Bayer filter mosaic [14]

Image Recording Equipment

The Nikon D3200 was purchased first, and it is an excellent consumer graded all-round DSLR camera. The reason for choosing this model was because the D3200, and cameras with similar specifications, are a popular choice for members of the public, namely hobby photographers and astronomers. The Nikon D3200 uses a 23.2x15.4 mm CMOS sensor with 24.2 million effective pixels (24.7 million total pixels). For this project an AF-S VR DX Nikkor lens with focal length of 18-55 mm and a maximum and minimum aperture of f/3.5-5.6 and f/22-36 was used, which was the standard lens delivered with the camera. All recordings, still and video were obtained with this lens. Still images were recorded in the Nikon Electronic Format (NEF), a RAW data format of 12-bit files for best results. Video files on the other hand were recorded in the file format .MOV as High Definition (HD) files at a quality of 1280x720 pixels with 50 frames per second (fps) in PAL video mode.

The Nikon 1 V1 was introduced later in the project for its slow-motion movie recording capability. This camera uses a 13.2x8.8 mm CMOS sensor with 10.1 million effective pixels. The Nikon 1 V1 was accompanied by two lenses. The 1 Nikkor VR lens with a focal length of 10-30 mm and a maximum aperture of f/3.5-5.6 and a 1 Nikkor VR lens with a focal length of 30-110 mm and a maximum aperture of f/3.8-5.6. Most recordings utilised the 1 Nikkor VR 30-110 mm because of the increased focal length, however later in the project an AF-S DX Nikkor lens with a focal length of 35 mm and maximum and minimum aperture of f/1.8 and f/22 was added. This lens was used in conjunction with the FT1 mount adapter. As with the D3200 all still images were recorded in the NEF format. However video recordings were recorded as .MOV files in a quality of 320x120 pixels with 1200 fps in the PAL video mode. Using this relatively high frame rate, the possible recording time was only 5 seconds which translated into a 3 minute and 20 seconds normal time movie. To use this feature in our experimental setup, an infrared remote control ML-L3 was purchased, and the camera was placed at the viewport 1 (Figure 10) of the impact chamber. This allowed unrestrictive communication between the camera and the remote control, while positioned in an adjacent room, during firing of the LGG. Figure 10 shows the different viewport configurations for recording of video footage and spectral recordings.

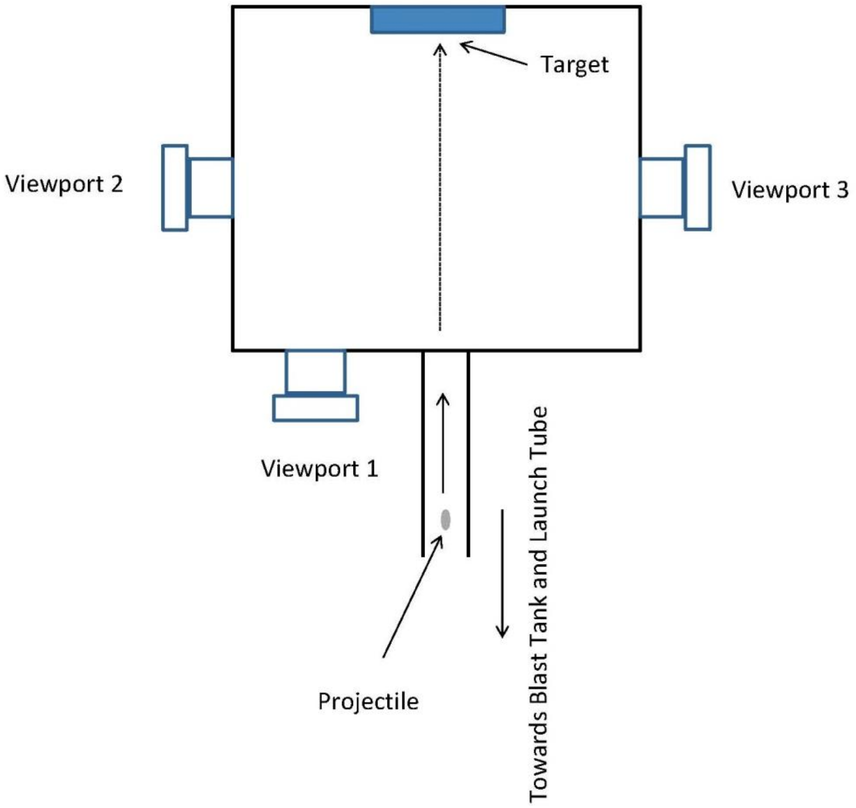

Figure 10: Viewport configuration of target chamber. (Top view)

At the start of this project, when only the Nikon D3200 camera was available, viewport 1 was used for imaging and viewport 2 for spectral recordings. This configuration was interchanged for the setup of the aluminium foil stack impacted by glass to have a side view of more than one foil (shot ID G231112#3 and G301112#2). After the Nikon 1 V1 became available the viewport 3 was used to set up both cameras for the same shot. The Nikon D3200 occupied viewport 3 for these impact experiments for the reason mentioned earlier. In order to avoid a trip hazard around the impact chamber on viewport 1 and 2 through the extended legs of a camera tripod, a special camera holder was designed by the author, which was able to clamp on to the target chamber as needed (see Figure 12) and was fully mobile in all three axes. For this an ordinary non-functional camera tripod was disassembled and the tripod head and telescopic section reused. A new holder plate was fabricated in the University workshop. Figure 11 shows the technical drawing of the holder plate made for the workshop and Figure 12 shows the camera holder in the final configuration with the Nikon 1 V1 camera attached at viewport 1.

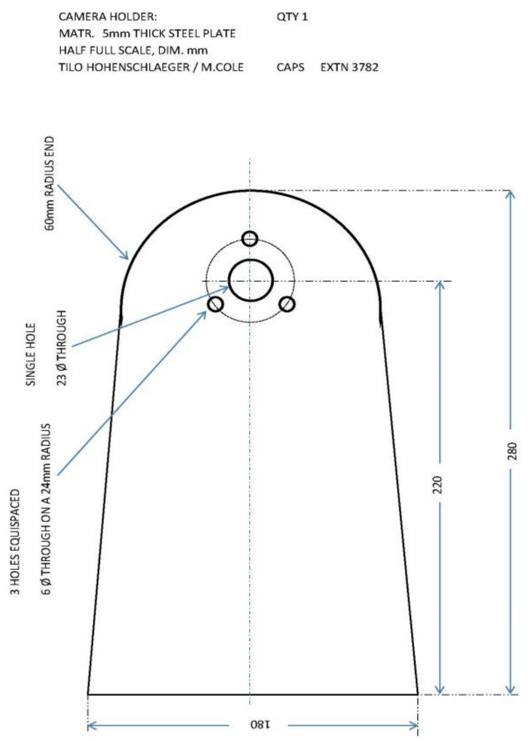

Figure 11: Technical drawing of camera holder plate.

Figure 12:Final configuration of designed camera holder

Camera Calibration

In order to use the images recorded for any quantitative work, the cameras' digital recording systems had to be characterised. For this a three step scheme was devised.

1.) Measuring the pixel colour response, by photographing a calibrated spectrum.

2.) Measuring the pixel intensity response, by plotting recorded intensity versus attenuation with neutral density filters.

3.) Measuring the pixel relative sensitivity, by photographing a test screen of equal brightness contours.

4.) Measuring the cameras sensitivity to infrared, by comparing the dark, IR, portion to the visible portion of the calibrated spectrum

1) Measuring the pixel colour response, by photographing a calibrated spectrum

The most common sources of visible light are transitions of the valence electrons in atoms [15]. In normal conditions the atom is in the ground state and all the electrons are in their lowest allowed energy levels. This must be consistent with Wolfgang Pauli's Exclusion Principle, which states that no more than one electron is allowed to occupy a given quantum state specified by the complete set of single – particle quantum numbers (n, l, m_l, m_s) [16]. If an atom absorbs electromagnetic radiation it is these valence electrons that are responsible for the energy changes that result in the emission or absorption of visible light.

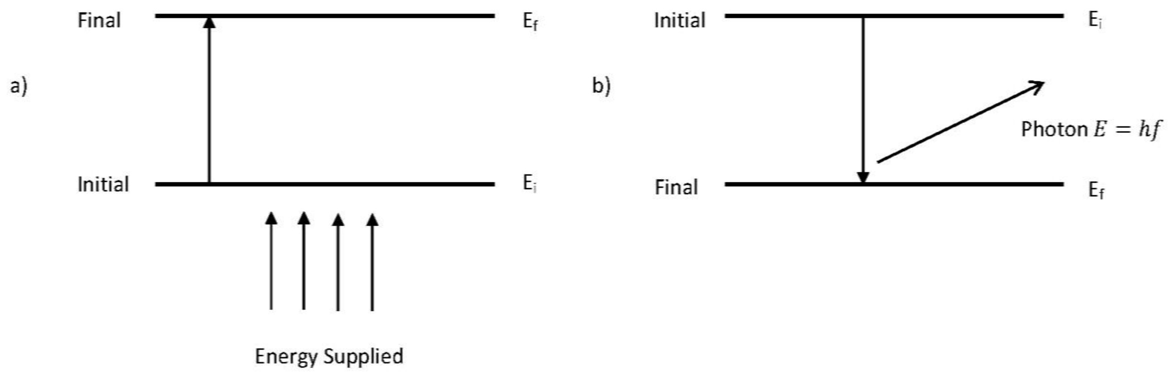

Figure 13: Diagram of energy transitions found during absorption (a) and emission (b)

Since $c = \lambda f$, where c is the speed of light (m s^{-1}), λ is the wavelength (m) and f is the frequency (Hz), the wavelength of the emitted light is then $\lambda = \frac{c}{f} = \frac{hc}{hf} = \frac{hc}{|\Delta E|}$. The change in energy ΔE = E_i - E_f and h is the Planck constant. It therefore follows that all atoms of the same element will have the same allowed energy transition and atoms of different elements will have different transitions and therefore different energies. From equation 2, it can be seen that different atoms will have different wavelengths of light produced by the emission spectra. For more complex molecular sources the same rule applies, as with atomic spectra each molecule will have a specific set of allowed transitions and so wavelengths. - When a beam of light is passed through a diffraction grating, a diffraction pattern for the maxima is produced due to constructive interference and is observed according to the equation $m\lambda = \frac{1}{n} sin\Theta$, where m is the order of diffraction (0, ±1, ±2…), n is the number of slits per meter and Θ is the angle of observation. For all the experimental work detailed herein a 600 line/mm grating in a standard 5 x 5 cm slide mount was used, on loan from the teaching laboratory. The emission tubes and the power supply were on loan from the South East Physics network (SEPnet) outreach officer. Figure14, 15 and 16 show these items.

Figure 14:Emission tube power supply

Figure 15: Emission tube

Figure 16:Diffraction grating

Photographing a calibrated spectrum proved more difficult when anticipated. At the beginning of the project low cost spectroscopes were used with little or no success. It was virtually impossible to photograph the spectral lines through these devices. Both spectroscope types are shown in Figures 17 and 18.

Figure 17:DVD grating spectroscope

Figure 18: Spectroscope

It became obvious that a different approach was needed. Early attempts to reflect the spectral lines of the emission tube on to a measurement grid did not work well either, or with unsatisfactory results.

Figures 19 and 20 show attempts at self-build spectroscopes and Figure 21 is an early image of a Cadmium emission lamp spectrum.

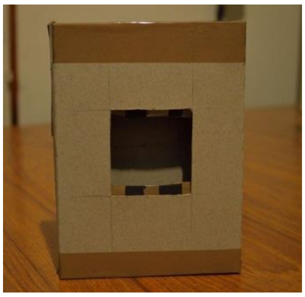

Figure 19: First attempt of self-build spectroscope

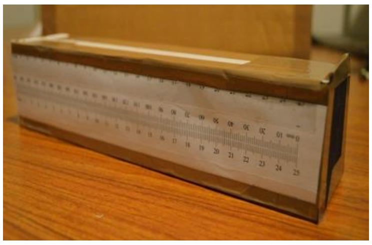

Figure 20: Self-build spectroscope with scale

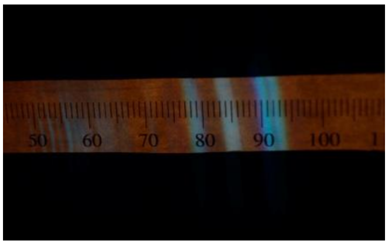

Figure 21: Attempt of photographing a Cadmium emission lamp spectrum

More research was needed and the solution came from a published article by Dr. Philip M. Sadler. The article, "Projecting Spectra for Classroom Investigations" [17] described the use of an overhead projector to visualise the spectrum of a lamp on a screen. This method was adapted for my own purpose as seen in Figure 22.

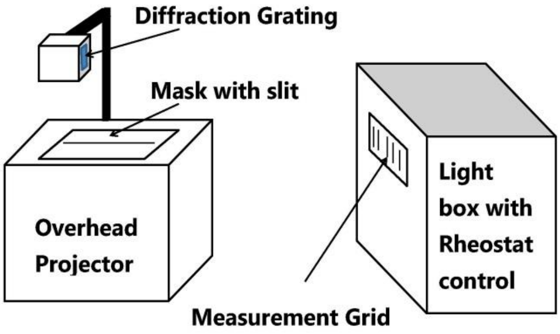

Figure 22: Modified experimental setup after Dr. PM Sadler

Figure 23: Slit mask

A slit mask was built to cover the entire glass top of the projector as well as the emission tube later on with a slit width of 3 mm ± 0.5 mm (Figure 23). To control the slit length, two A4 pages of black paper were employed.

To use the power supply with the emission tubes for the same purpose, a cover box which encases the unit was made (Figure 24). Finally a light box with an integrated mm ruler and a rheostat which controlled the light intensity was built (Figure 25).

Figure 24:Cover box for power supply

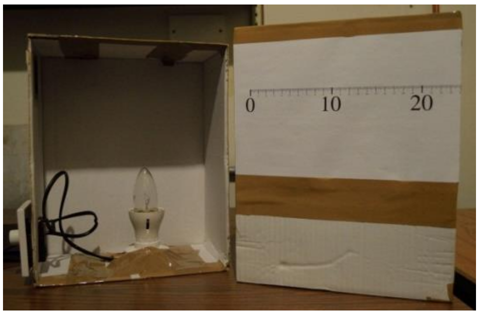

Figure 25: Light box with rheostat control

Printable mm rulers are available in the Portable Document Format (PDF) on the Internet [18]. To ensure accuracy of the printed ruler, the "shrink to fit" option has to be disabled otherwise the reproduced ruler will be distorted. Figure 26 shows the complete setup of the components as utilised in the image recording. Figure 27 were recorded using the described method.

Figure 26: Completed setup of all components

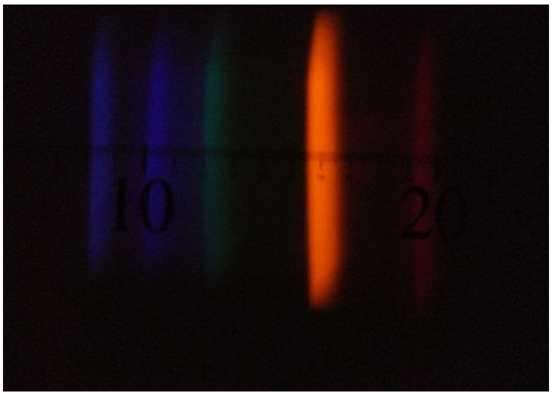

Figure 27: Recorded spectrum of a helium emission tube

To record an image that can be used for the mentioned task earlier, the image must not be overexposed or saturated. For both cameras the following formula for the exposure was used:

$$Exposure \approx \frac{1}{f^2}\ x\ t\ x\ iso\ x\ mv^2 \qquad \text{Eqn. (4)}$$

were f is the cameras aperture number, t is the shutter speed of the camera (exposure time in seconds), iso is the CCD sensitivity setting of the camera and m and v are the mass in kg and velocity of the projectile in m s^{-1} respectively.

2.) Measuring the pixel intensity response, by plotting recorded intensity versus attenuation with neutral density filters.

For this procedure a set eight different neutral density filters were used. These were filters with a light transmission of 63.096%, 39.811%, 25.119%, 15.8849%, 10%, 1.0%, 0.1%, and 0.01%. A series of photographs were taken of the same light source while reducing the light transmission via the filters. These images were analysed using the same pixels in each photograph.

3.) Measuring the pixel relative sensitivity, by photographing a test screen of equal brightness contours.

A white projector screen was photographed for this step.

4.) Measuring the cameras sensitivity to infrared, by comparing the dark, IR, portion to the visible portion of the calibrated spectrum

Due to time constrains and the delays in the project this step was not carried out.

Software

To keep the costs of the project down all the video and image manipulation was carried out without the aid of expansive software packages. Where possible, freely available software was used, which can be downloaded from the internet. When acquiring the two Nikon cameras, the software delivered with these items is called ViewNX2. This software was used for all the related work with the RAW data and compressing the data to the Joint Photographic Experts Group (JPEG) format, except for the video footage. To extract images from the video footage taken, alternative software is required. During the research, several different free software packages were examined. Because of the quick and intuitive handling the VideoPad Video Editor from NCH Software [19] was chosen for the task. The downside of processing the data this way was the restrictive quality of the exported images, which only could be saved in either the JPEG format or the Portable Network Graphics (PNG) format. This resulted in data reduction of the original recorded image and therefore image quality loss.

USB650 Spectrometer

Using the camera calibration technique for recording impact flash spectra was the next logical step. However because of the difficulties described earlier, it was decided to use other means of recording spectral data. For this reason the USB650 Spectrometer by Ocean Optics was introduced to this project. This was on loan from the teaching laboratory and included the operating software called - “SpectraSuite” - which was run on a Windows XP notebook while acquiring data and connected via the Universal Serial Bus (USB) as well as a fibre optical cable as seen in Figure 28. It has a detector range from 200-1100 nm and uses a linear silicon CCD array with 2048 pixels. For all spectral recordings an integration time of 100 milliseconds was used.

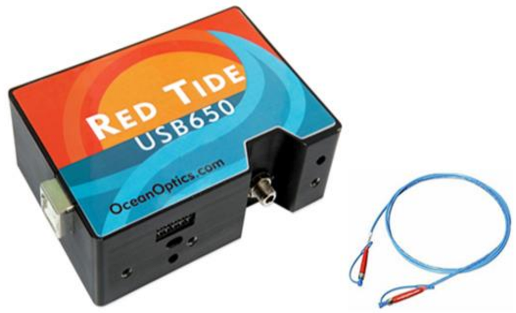

Figure 28: USB Red Tide Spectrometer with optical fibre cable

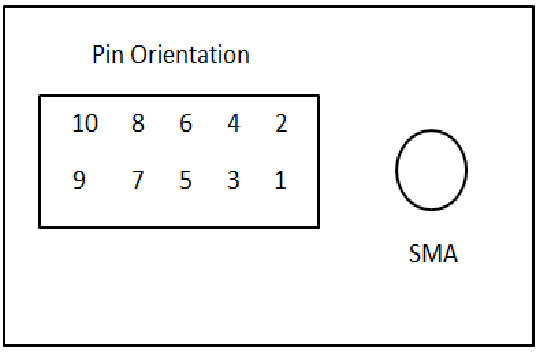

Figure 29: 10- Accessory Connector Pin-out Diagram

Running the spectrometer during impact shot firings, the unit was set in the external trigger mode connected via pin 7 and grounded via pin 6 (see pin configuration in Figure 29), and then triggered by the impact sensor of the stop plate, as mentioned earlier. This sensor is made of polyvinylidene difluoride (PVDF). When this material is flexed by the shock wave of the stop plate, an electrical signal is produced and transmitted and triggers the spectroscope. After recording the spectra, the data sets were exported into a word processor for easy use of the data. For interpreting the resulting graphs the National Institute of Standards and Technology (NIST) was consulted [20].

Results

36 hypervelocity impacts have been attempted to record with a various degree of success. To date, video recordings with the Nikon 1 V1 were of such poor quality that any effort to get any meaningful data failed. For this matter only the calibration data for this camera is presented in this section.

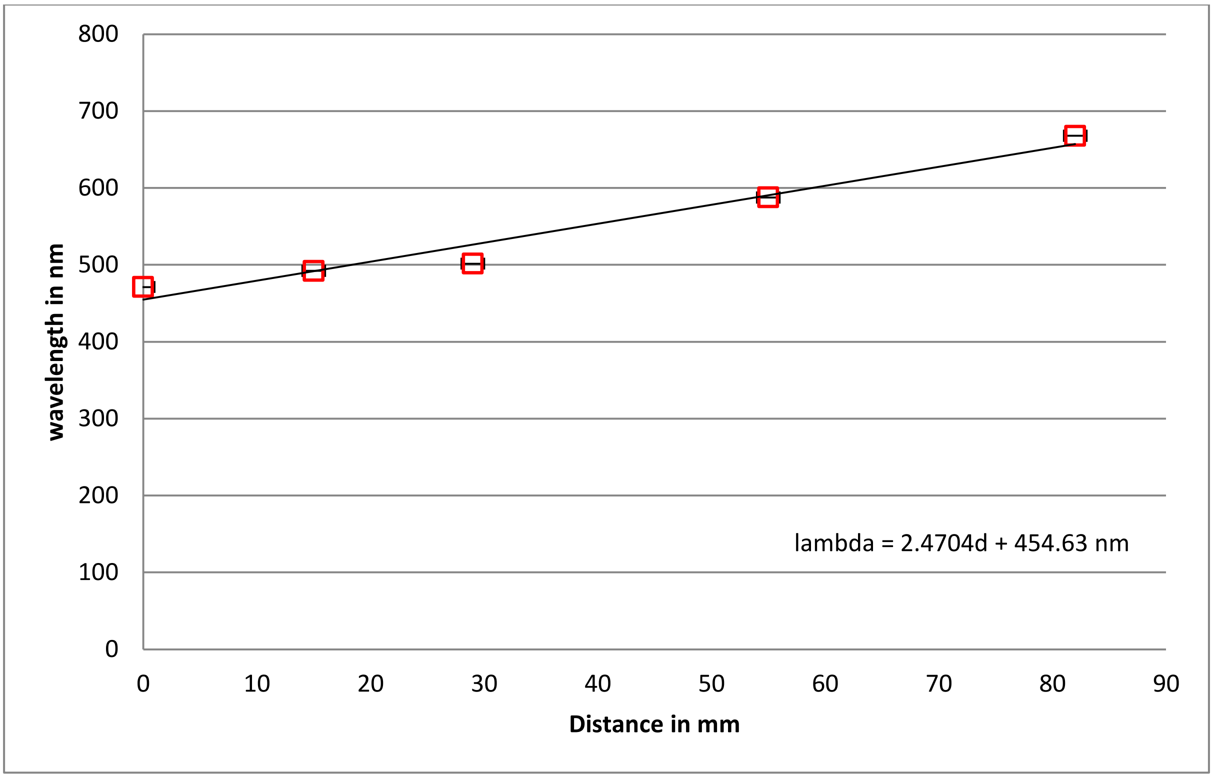

Figure 30: Distance versus wavelength calibration using a helium emission tube. The data points correspond to the major emission lines of helium

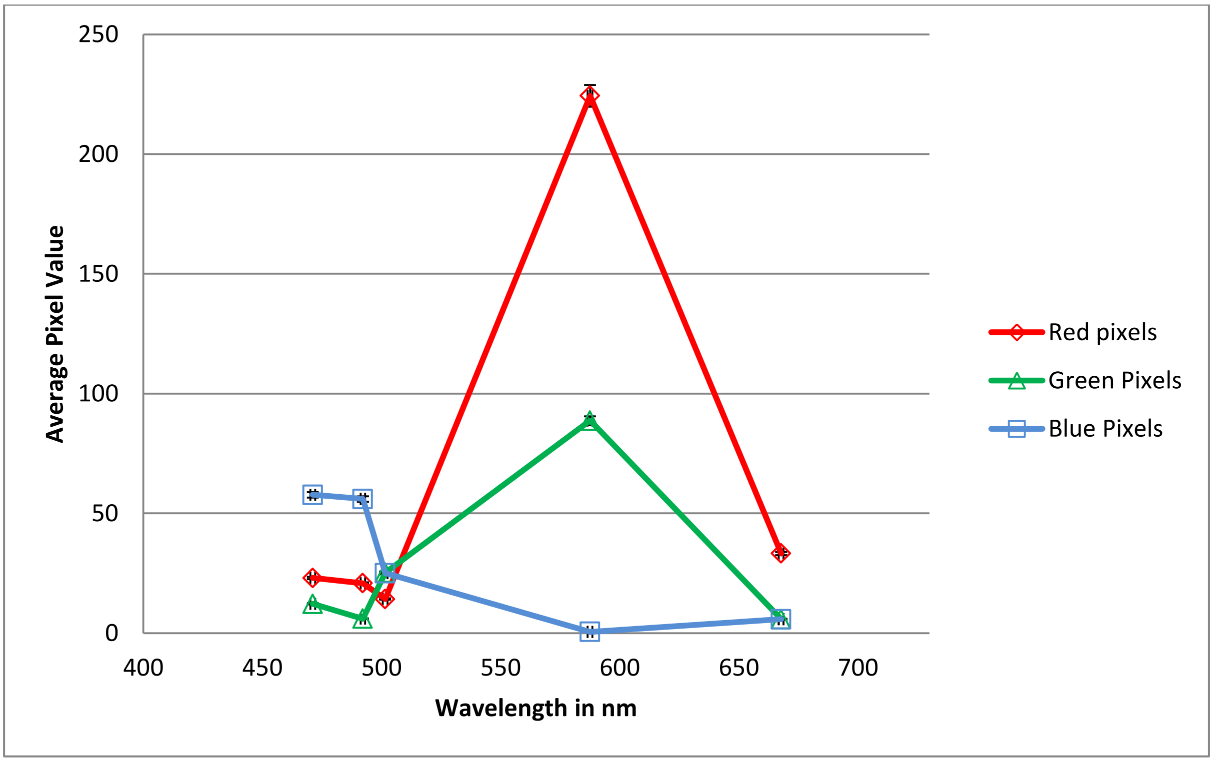

Figure 31: Wavelength versus average pixel value for the Nikon 1 V1

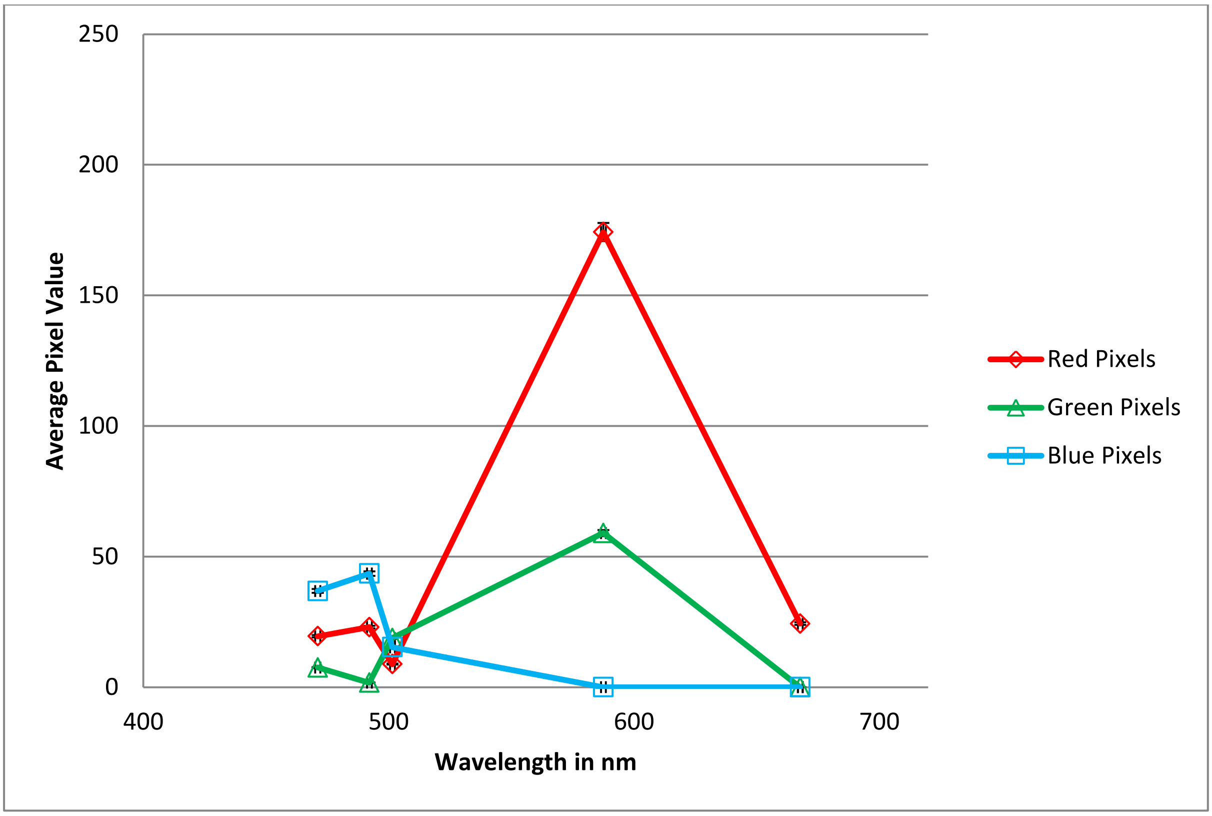

Figure 32: Wavelength versus average pixel value for the Nikon D3200

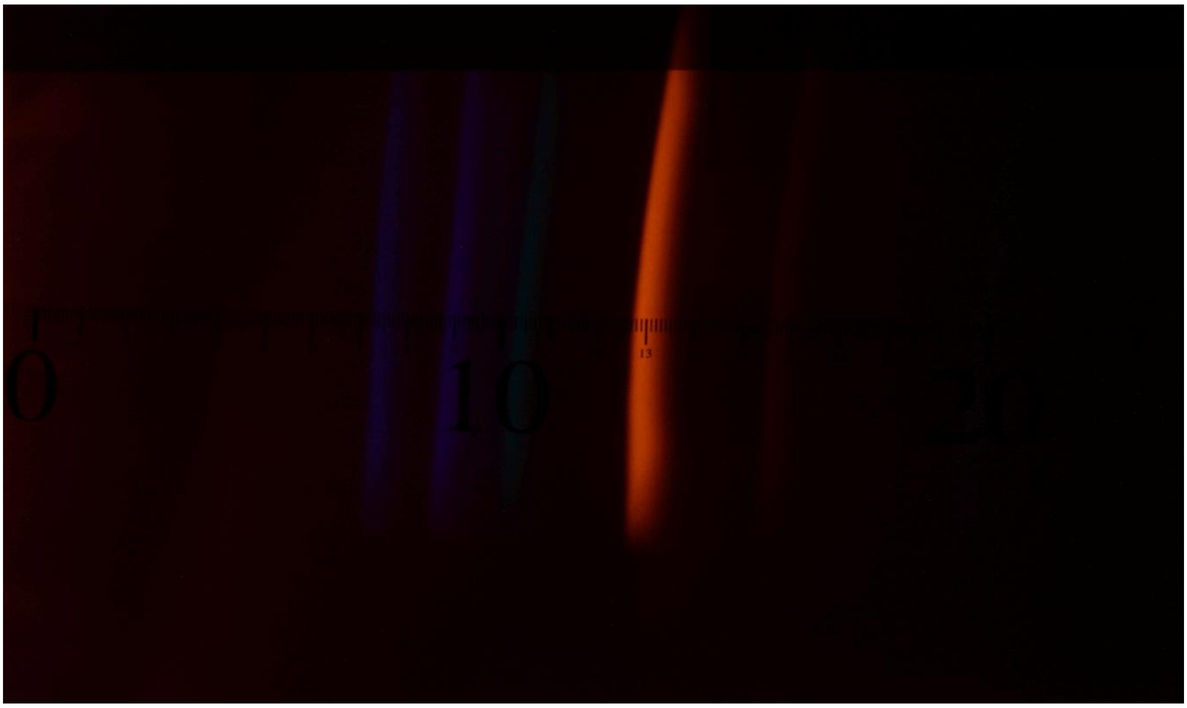

Figure 33: Helium spectrum photograph for comparison.

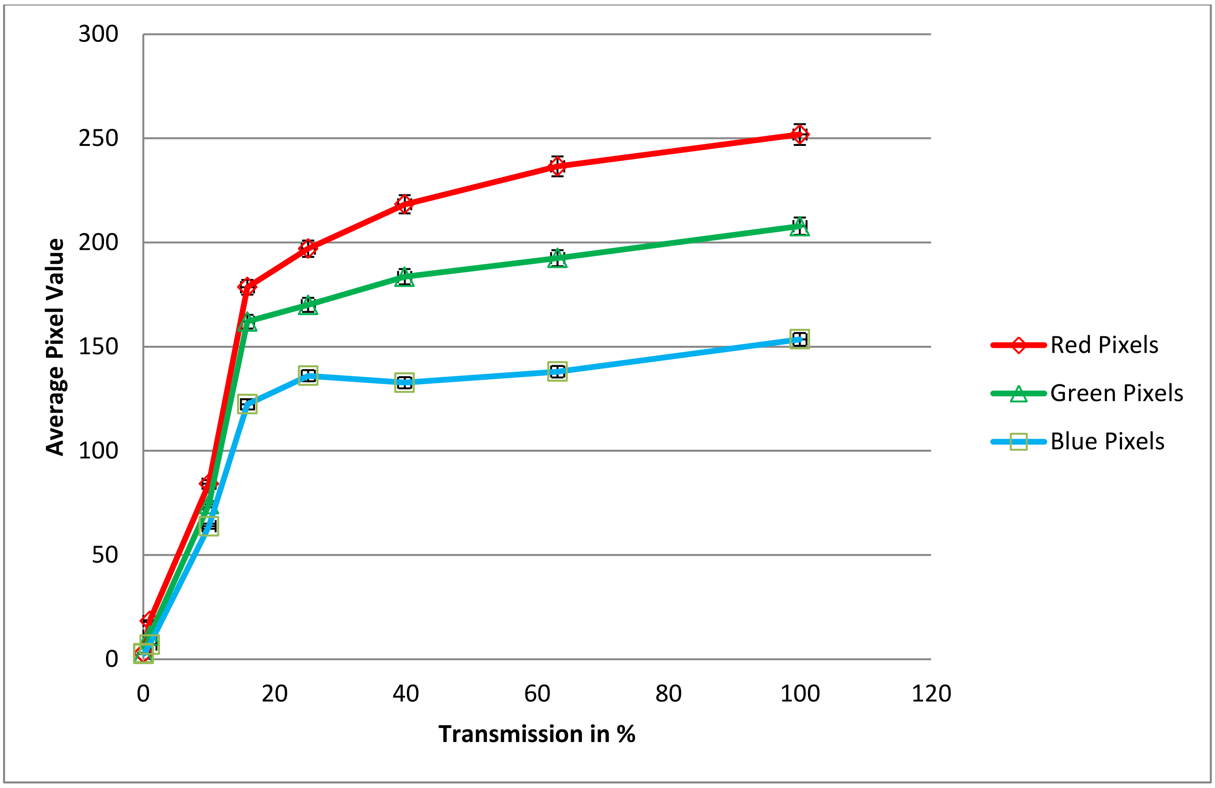

Figure 34: Neutral density filter attenuation versus average pixel value for the Nikon 1 V1

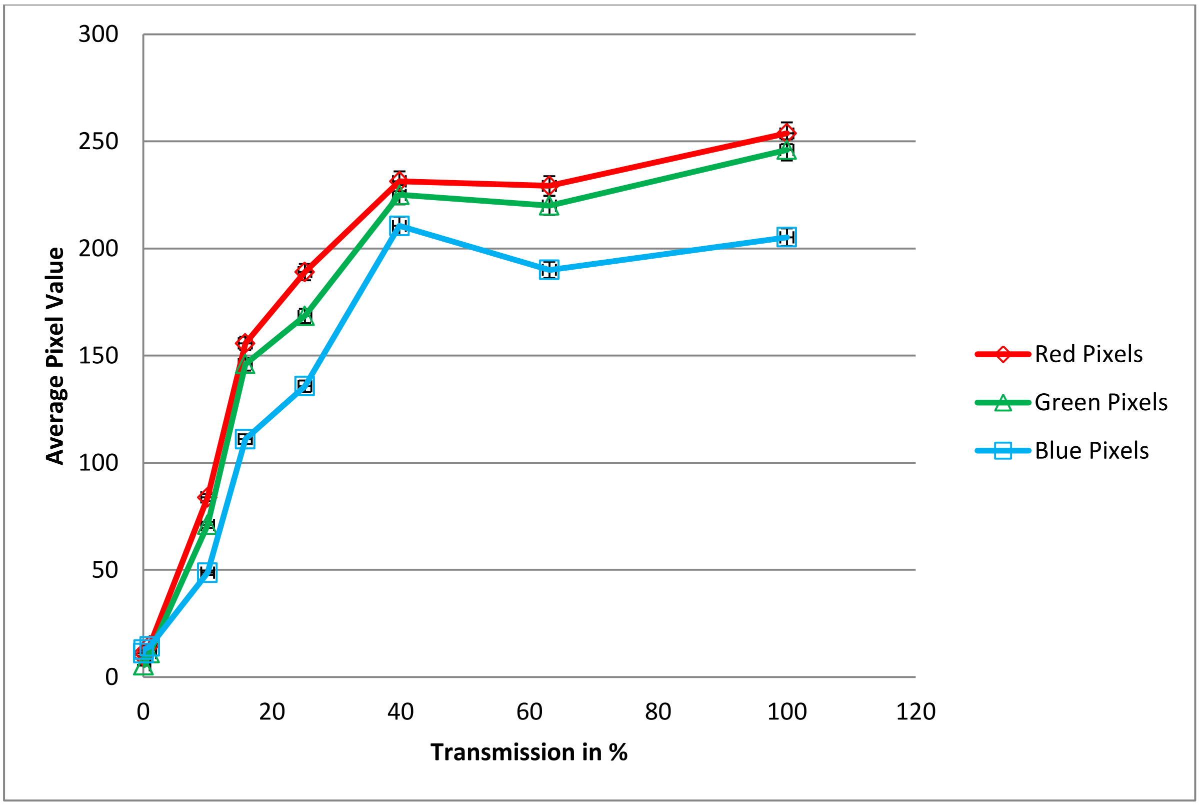

Figure 35: Neutral density filter attenuation versus average pixel value for the Nikon D3200

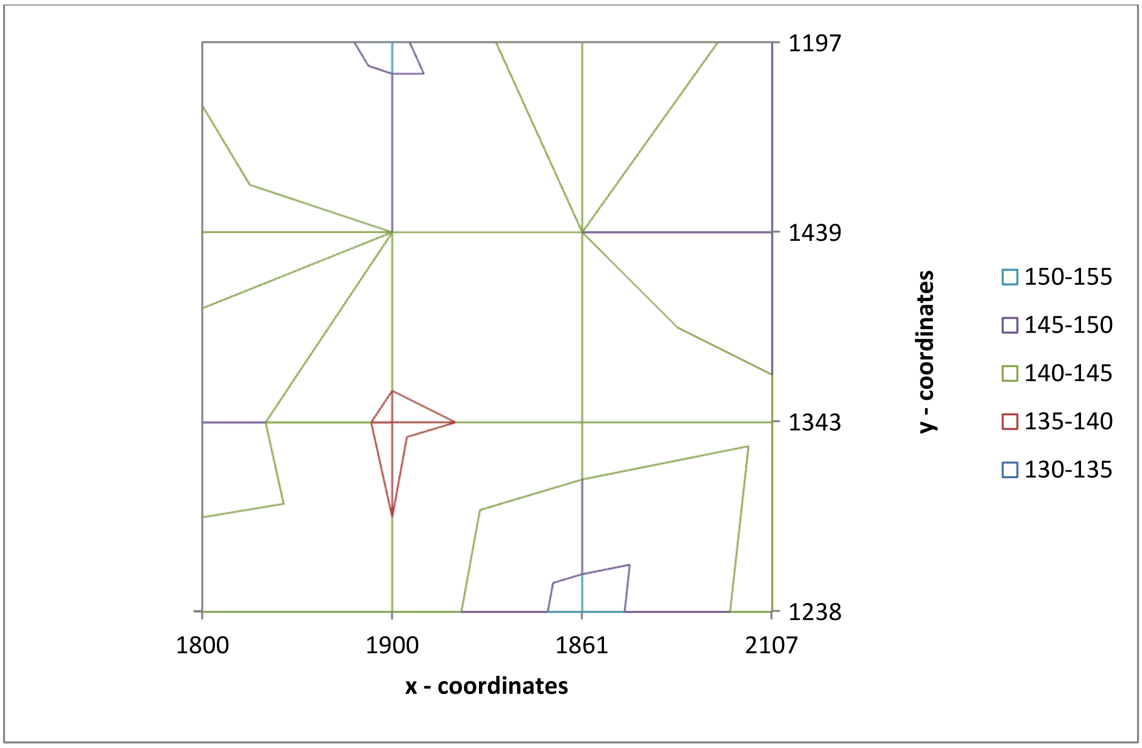

Figure 36: Brightness contours of red pixels for the Nikon 1 V1

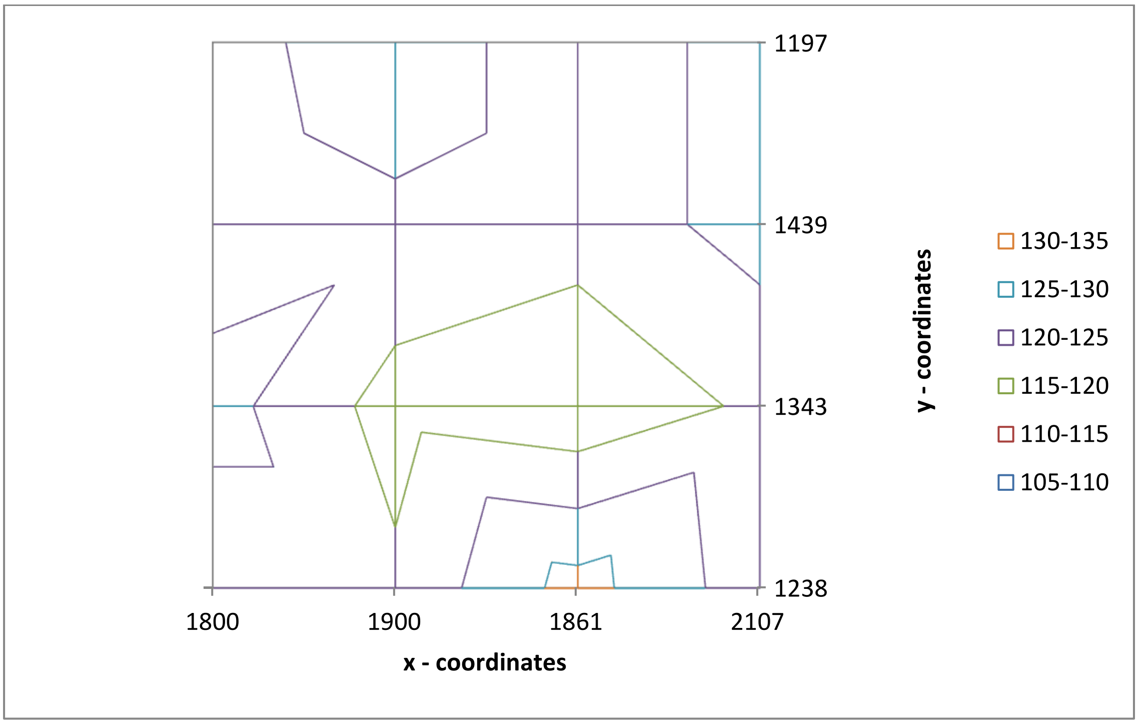

Figure 37: Brightness contours of green pixels for the Nikon 1 V1

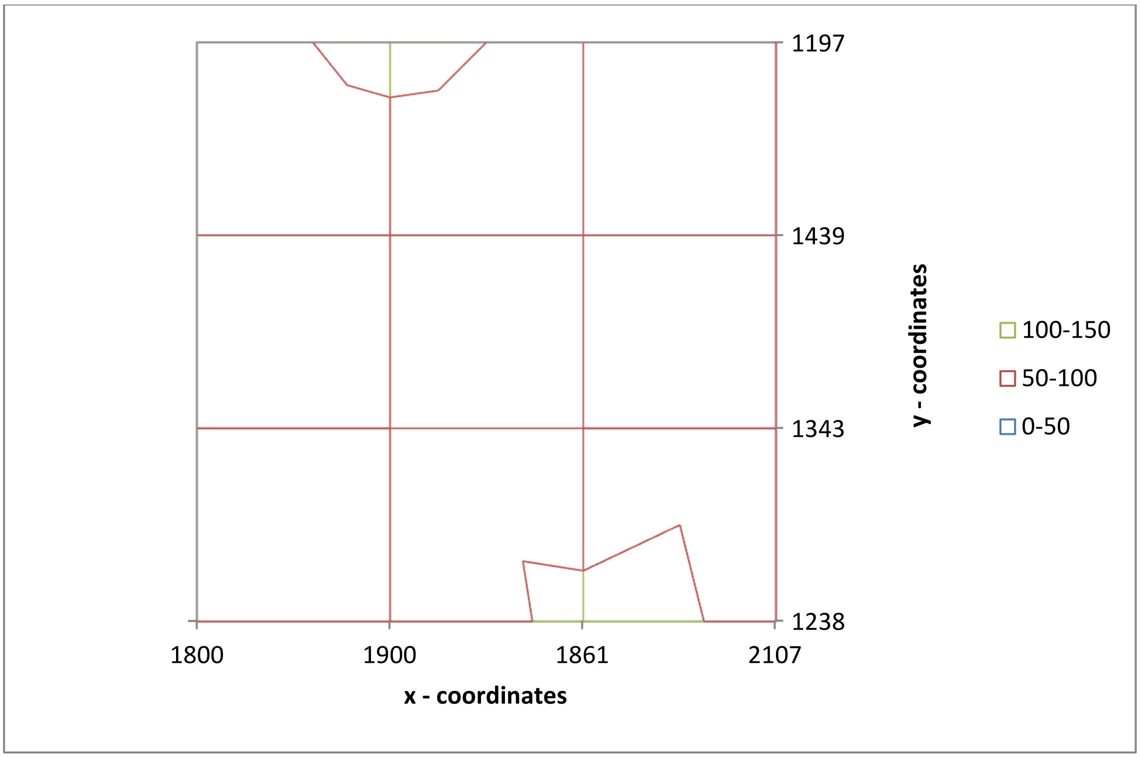

Figure 38: Brightness contours of blue pixels for the Nikon 1 V1

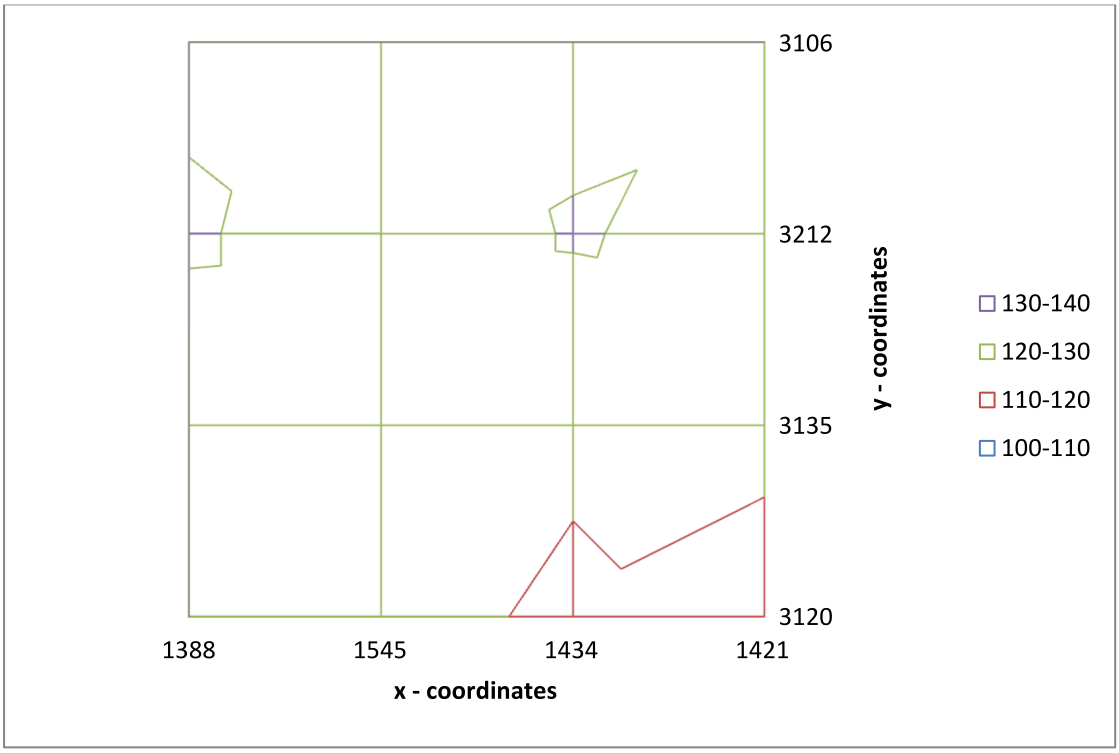

Figure 39: Brightness contours of red pixels for the Nikon D3200

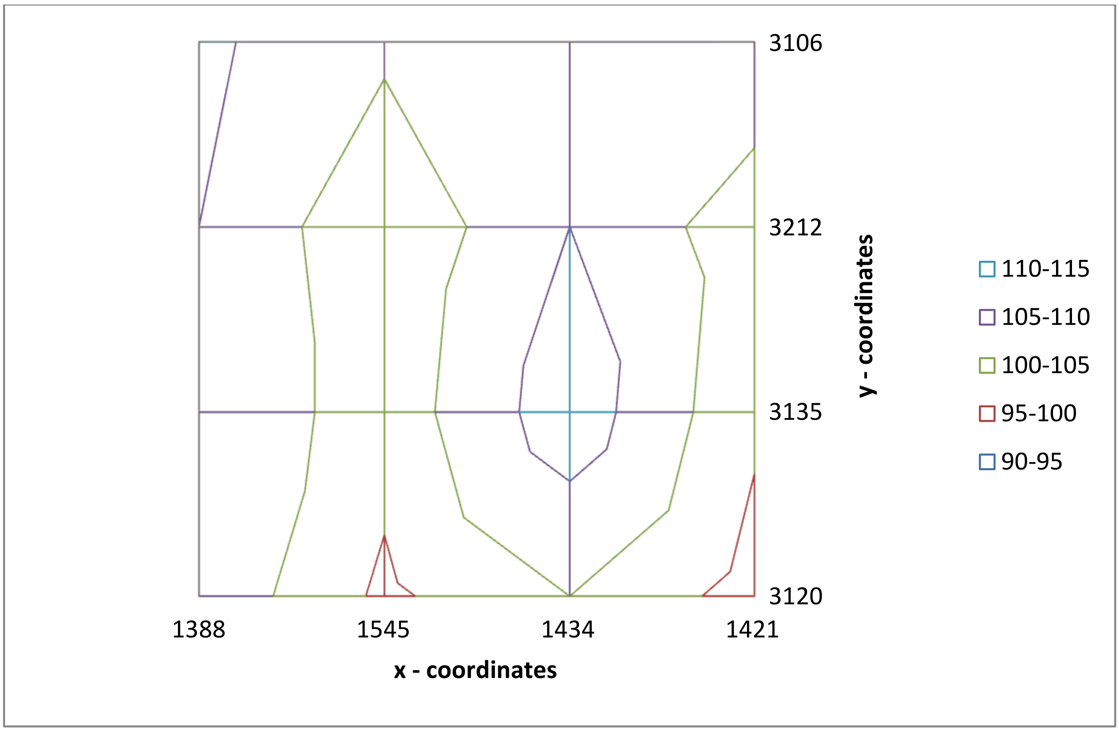

Figure 40: Brightness contours of green pixels for the Nikon D3200

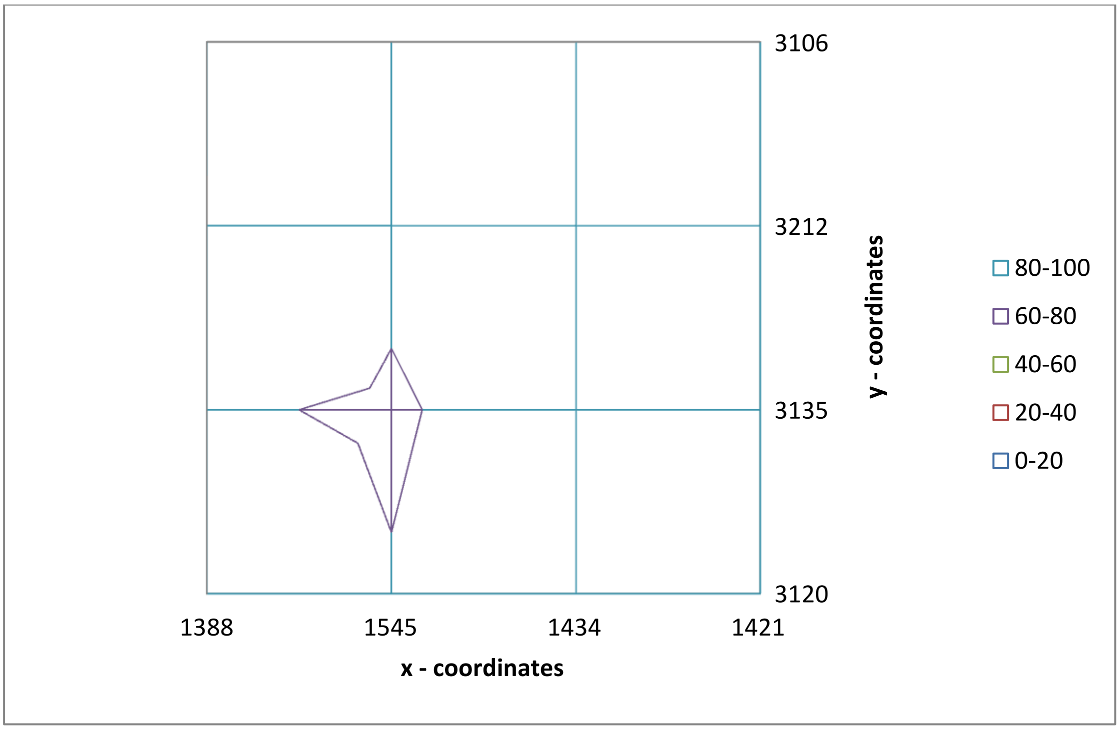

Figure 41: Brightness contours of Blue pixels for the Nikon D3200

USB650 Red Tide Spectrometer data

As this hardware became only available after the programme had already been started and accounting for problems encountered during the use of the equipment, 8 spectra had been collected. Obstacles related to the software were overcome by updating the system software itself and early or non-trigger events were solved by the use of the PVDF sensor as well isolating the system from the main power supply. The results are shown in the Figures 44, 45 and 46. The graphs show the wavelength in nanometres (nm) versus the Log_{10} of the intensities (counts) measured. The spectra are grouped for the same impactor and target materials used. Since the spectrometer recorded the wavelength only in whole number steps and the NIST website provides data measurements with accuracy, in some cases with more than five significant figures, the data presented includes the closest matches of ±0.5 nm to the whole wavelength.

To complement and clarify the results shown hear estimates of the impact parameters, peak pressure (P_{peak}), and the peak post-shock temperature (T_{pps}) were calculated. Calculating these, input of experimental Hugoniot data for projectile as well as target and various material properties of the projectile, like heat capacity, are required. To determine the peak pressure, the graphical method outlined in Melosh [21] was used. Here, a plot of pressure (P) in GPa, against particle velocity (u) in km s^{-1} is constructed from available Hugoniot data for the Aluminium target, plotted forward from $u = 0$ at $P = 0$ and the nylon projectile plotted backward from $u =$ the impact velocity at $P = 0$. At the point where these two curves intersect corresponds to the P_{peak} to the nearest GPa. Hugoniot data for the Aluminium 6061, nylon, and Polytetrafluoroethylene (PTFE) were obtained from a reference table by Marsh [22]. Figures 42 and 43 are showing two examples for this graphical method. Figure 42 is for the shot ID G021112#2 representing a nylon projectile impacting an aluminium plate with a speed of 6.32 km s^{-1} and Figure 43 is for the shot ID G300113#1 representing a PTFE projectile impacting an aluminium plate. Note the different points where both lines intersect for the two different materials.

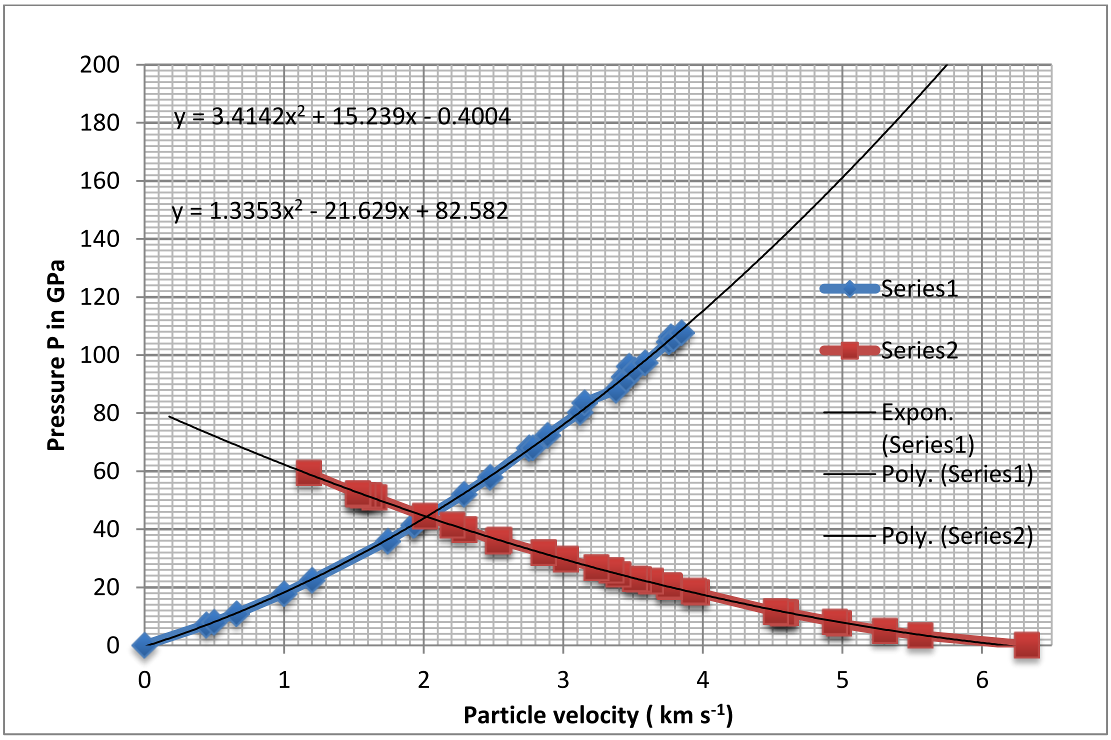

Figure 42: Particle velocity u versus pressure P for shot ID G021112#2

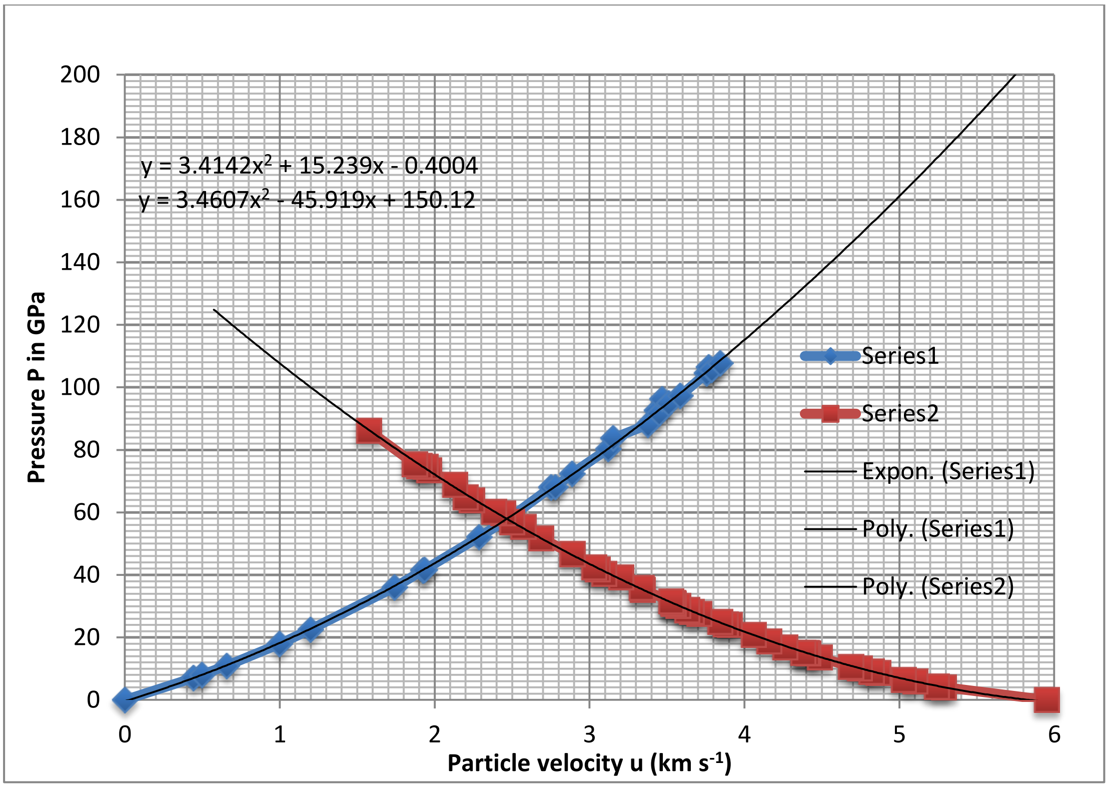

Figure 43: Particle velocity u versus pressure P for shot ID G300113#1

The peak post-shock temperature is the temperature of the decompressed shocked material that results from waste heat deposited after shock and release [23]. This was estimated using the method by Artemieva and Ivanov [24] as well as Fritz et al. [25]. The peak post-shock temperature is expressed as:

$$T_{pps} = T_0 + \frac{u_{max}^2 - 2\,E_R}{2\,C_p} \qquad \text{Eqn. (5)}$$

where T_0 is the pre-shock temperature of the material (300 K), u_{max} is the maximum particle velocity experienced in the projectile (in m s^{-1}), E_R is the energy lost from the projectile during release from high pressure (in J) and C_p is the specific heat capacity of the projectile (in J kg^{-1} K^{-1}) [23]. u_{max} was determined from the plot of u against P. The values of C_p used for Aluminium was 895 J kg^{-1} K^{-1} [26], 1700 J kg^{-1} K^{-1} for Nylon [27], and 1010 J kg^{-1} K^{-1} for PTFE [28]. E_R is approximated by assuming that the release occurs along the Hugoniot curve is adequately represented by a linear shock-particle velocity relationship of the form of:

$$U = c + su \qquad \text{Eqn. (6)}$$

where U is the shock velocity and c and s are constants [23]. Therefore

$$E_R = \frac{c}{s}\left(u_{max} + \frac{c}{s}\ln\frac{c}{U_{max}}\right) \qquad \text{Eqn. (7) [25]}$$

where U_{max} is the maximum shock velocity. Plotting values of U against u, taken from the Hugoniot data sources referenced earlier the values for c and s can be derived. Inserting these and assuming $u = u_{max}$ into Equation 6 will yield results for U_{max} and therefore E_r. All these values found can than substituted into Equation 5 to find the post-shock temperature [23]. The table 1 shows the calculated values for the impacts of nylon on aluminium and PTFE on aluminium plates.

Table 1: Calculated values of peak pressure and peak temperature for the impacts of nylon on aluminium and PTFE on aluminium

Shot ID: G021112#2							
	P_{peak} (GPa)	T_{pps} (K)	u_{max} (m s^{-1})	U_{max} (m s^{-1})	c (m s^{-1})	s	E_R (J)
Nylon	44	3107.4	4297.5	8934.0	3257	1.321	4.46 x 10^6
Al	44	866.9	2024.1	8042.3	5322	1.344	1.54 x 10^6

Shot ID: G071112#3							
Nylon	46	3300.9	4415.7	9090.1	3257	1,321	4.64 x 10^6
Al	46	920.5	2092.2	8134.0	5322	1.344	1.63 x 10^6
Shot ID: G231112#2							
Nylon	48	3497.2	4531.5	9243.0	3257	1.321	4.83 x 10^6
Al	48	976.1	2159.3	8224.1	5322	1.344	1.73 x 10^6
Shot ID: G141212#2							
Nylon	36	2366.9	3797.1	8273.0	3257	1.321	3.70 x 10^6
Al	36	673.7	1738.9	7659.1	5322	1.344	1.18 x 10^6
Shot ID: G300113#3							
Nylon	34	2191.1	3664.0	8097.2	3257	1.321	3.50 x 10^6
Al	34	630.9	1664.1	7558.6	5322	1.344	1.09 x 10^6
Shot ID: 300113#1							
PTFE	58	9180.7	4934.1	10257.4	1761	1.722	3.20 x 10^6
Al	58	1283.0	2479.4	8654.3	5322	1.344	2.19 x 10^6

It is to note that this method is not viable for the impacts of glass on aluminium foils since Hugoniot data does not apply for thin foils. For that reason the data regarding nylon impacting on aluminium is not included.

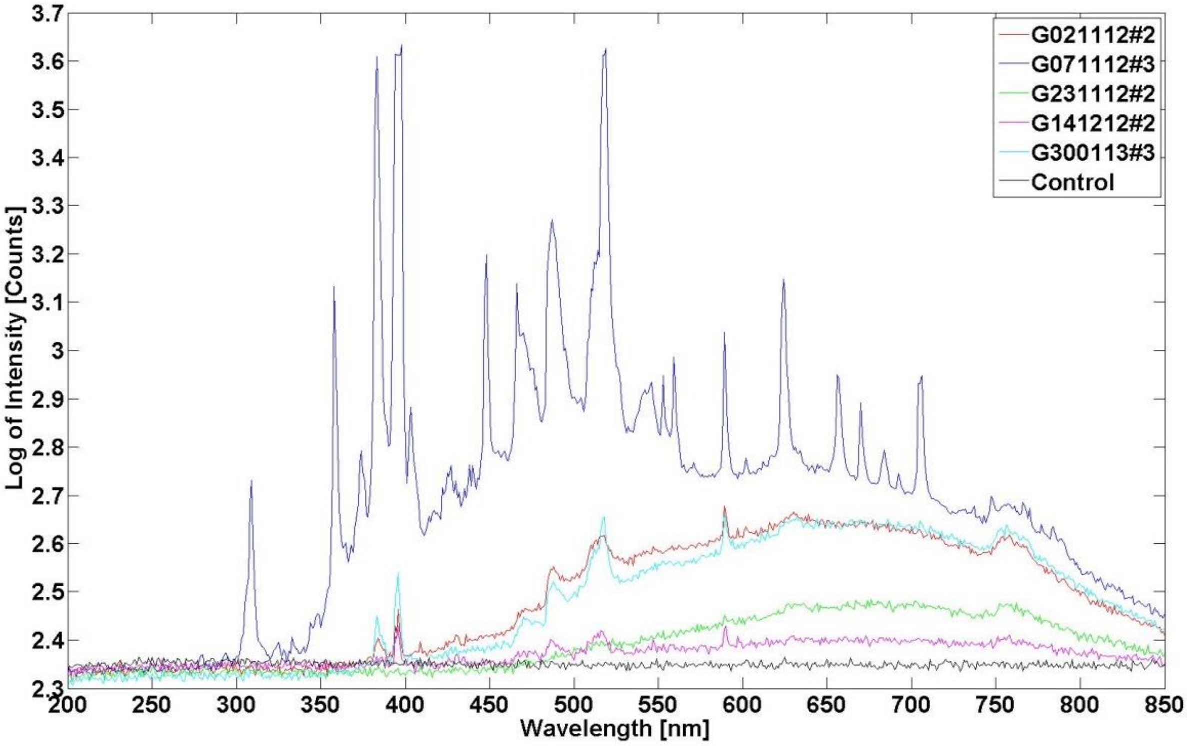

Figure 44: Impact spectra of nylon projectiles impacting on aluminium plates

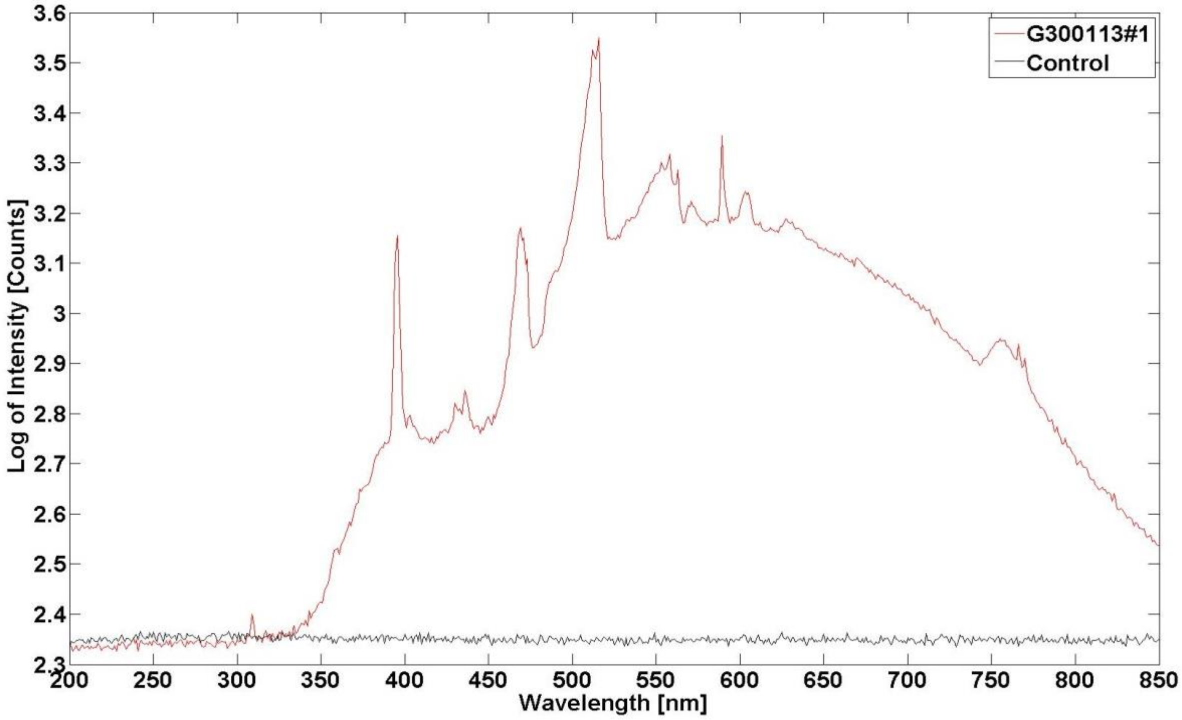

Figure 45: Spectrum of PTFE projectile impacting on aluminium plates

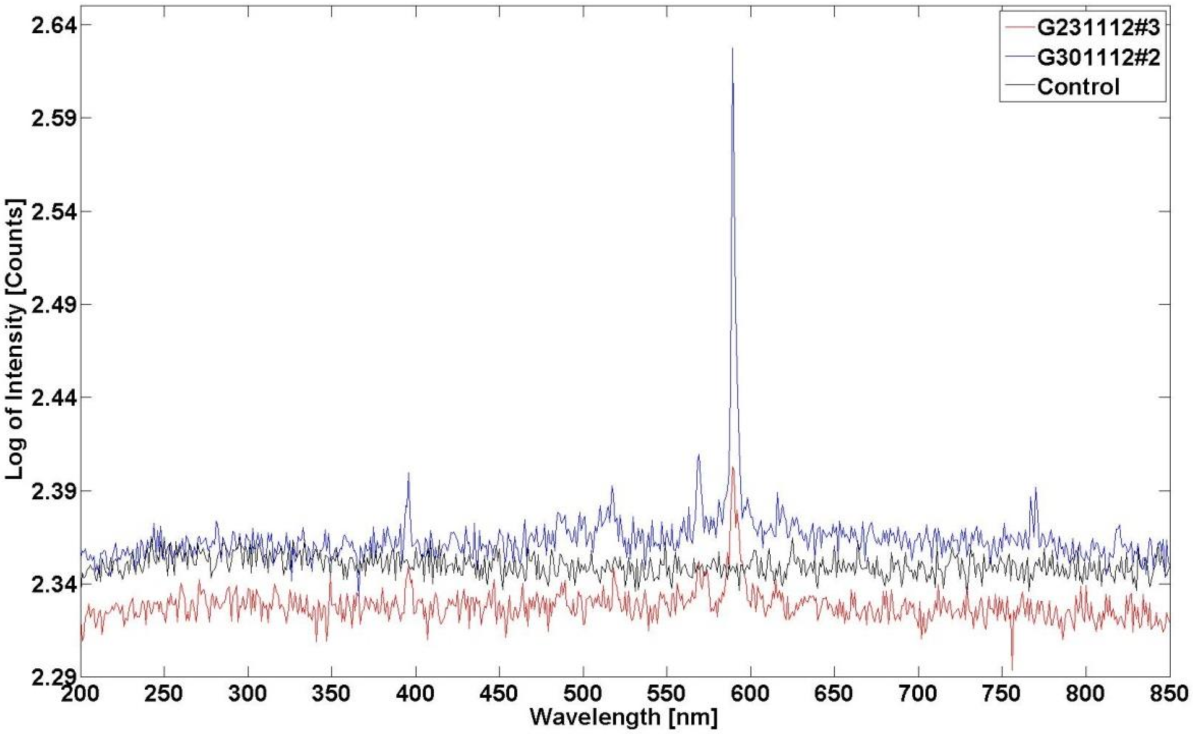

Figure 46: Spectra of glass projectile impacting on aluminium foils stacks

Discussion

Wavelength calibration

As shown in Figure 30 a linear relation was found as expected for the dependence of the wavelength and distance. Through this, the equation of a straight line of λ = 2.4704 d + 454.63 nm was obtained. This can be used as a tool for identifying emission lines of unknown spectra. One can observe an unknown emission spectrum of a hypervelocity impact flash through a slit, projected on to the mm scale screen, and would be able to calculate the observed wavelength. However this procedure was not performed due to the delays with developing the setup and the substitution of the spectrometer mentioned above. During the project it was found that the standard glass viewports are opaque to IR radiation. Figure 47 shows the viewport manufacturer [30] optical transmission curve for the glass used. To overcome this obstacle the decision was made to purchase a sapphire viewport for an extended transmission range. This range is shown in Figure 48.

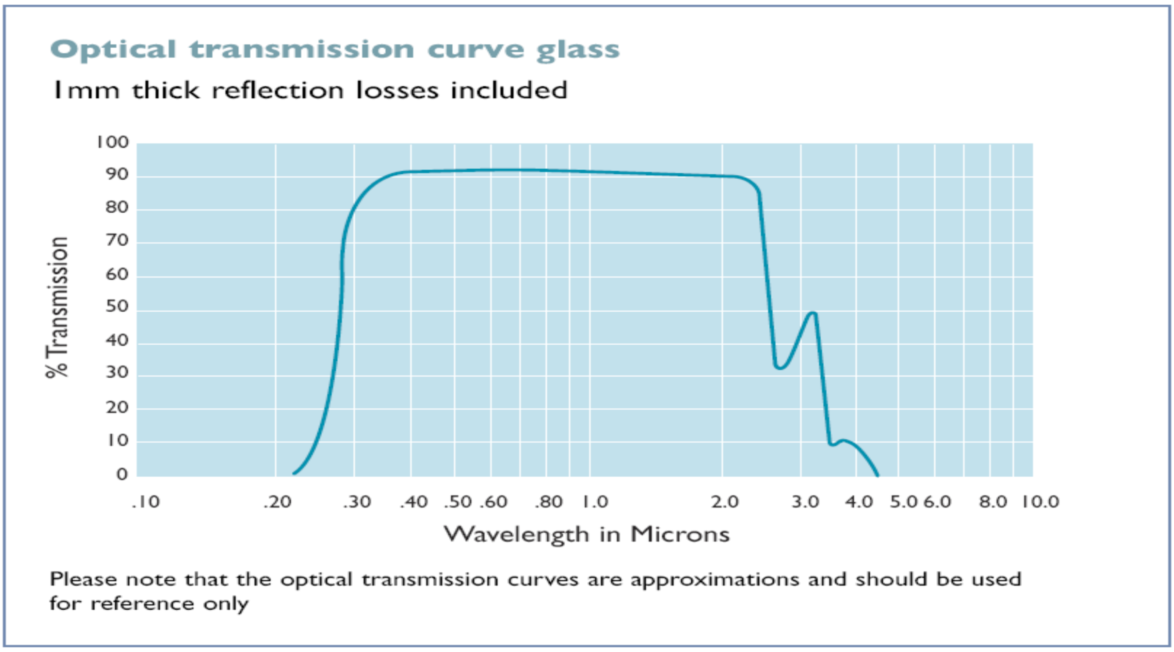

Figure 47: Optical transmission curve for glass viewport

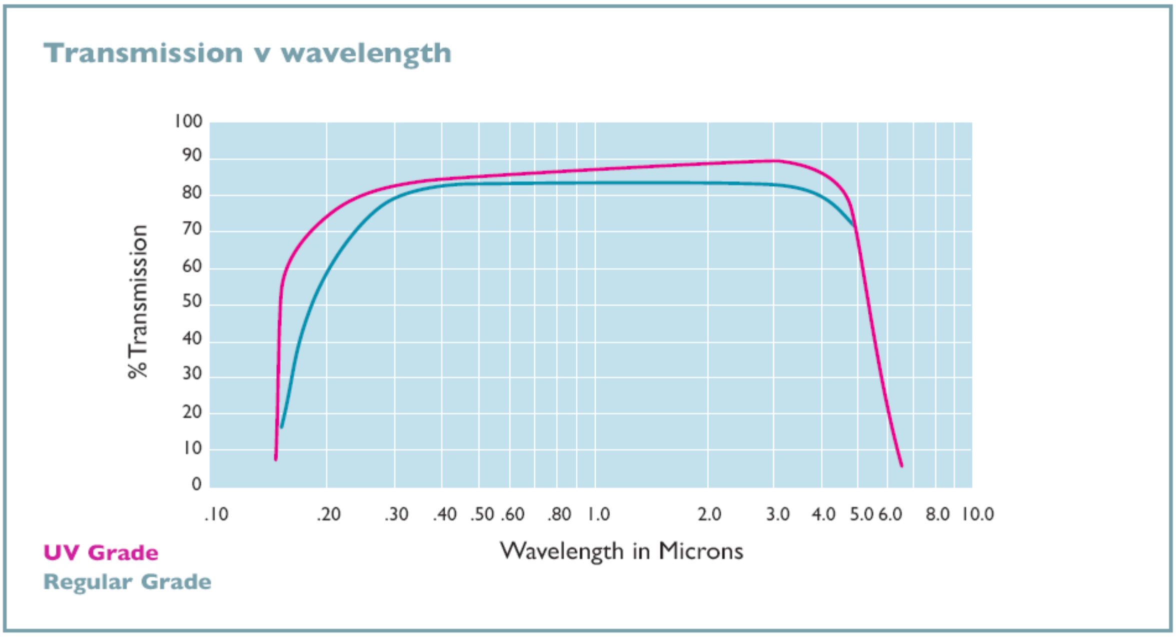

Figure 48: Optical transmission curve for sapphire viewport

Gain calibration

Plotting the average pixel value against the wavelength for both cameras as shown earlier, yields the relative response of the pixels to a certain wavelength. As it can been seen from the highest peak on Figures 31 and 32, the CCD is sensitive to yellow light, which is probably a result of manufacturing the CCD chip with the aim to reproduce colours to match the human eye using the earlier described Bayer filter. Comparing the two plots for both cameras, one can see that both CCD chips have a very similar pixel colour response. Coming from the same manufacturing company and using similar or identical components for these cameras is the obvious reason for that. Figures 34 and are showing the average pixel value plotted against the attenuation from neutral density filters for both cameras. These plots are a measure of the pixel intensity response to a certain value of transmitted light. The transmission (T) in percentage is related to the optical density (OD) of the material by the following equation:

$$T = 10^{-OD} \text{ x } 100 \qquad \text{Eqn. (8)}$$

Giving this relation, a perfect sensor should exhibit a power law graph when plotted. However both cameras are not perfect instruments and display a different behaviour for the intensity response. The Nikon 1 V1 shows a sharp drop at 20 per cent of transmission, which indicates that the pixels becomes insensitive at that value of transmission. The Nikon D3200 on the other hand shows a more “real” response in the sense of a closer approximation of the plot to the idealised power law. Certainly it is a qualitative measure for the camera in use and probably explains partly the difficulties in producing usable image data for the Nikon 1 V1.

CCD spatial gain variation

Figures 36, 37, 38, 39, 40 and 41 illustrate the spatial distribution of the sensitivity of the CCD for both cameras. It shows that the sensitivity varies of approximately ±10 per cent in relation to the position on the CCD chip. The reason for this irregularity is probably due to variations in the Bayer filter mask. It is to note that only a small pixel area was sampled and given the number of pixels, 24.2 million and 10.1 million pixels for the Nikon D3200 and Nikon 1 V1 respectively, it is only a crude approximation.

All this work involving the calibration of the cameras so far presented was carried out using images in the RAW format, which will give the highest possible image quality. However, introducing video recording capabilities with both cameras has also a negative side effect on the images obtained. Extracting single images from the recorded video files using technology freely available, without increasing the overall costs of the project, it was only possible to save these images to a compressed file format. This means essential data is lost and could lead to inaccurate results. For this reason an error analysis was needed. To investigate the error involved, a RAW format image was converted to the JPEG format and analysed. The known pixel values from the RAW data were directly compared with the pixel value at the same coordinates of the JPEG format image. This procedure provided the following results. For the Nikon 1 V1 the red pixels showed a 27 % error in the average pixel value compared to the RAW data, the green pixels showed a 36 % error in the average pixel value compared to the RAW data, and the blue pixels showed a 12 % error in the average pixel value compared to the RAW data. Table 2 shows the pixel values for the RAW and compressed data for the Nikon 1 V1. For the Nikon D3200 the error values calculated for the red, green and blue pixels were 16.4%, 42.7%, and -2.7% respectively. In the case of the blue pixels a negative value indicates an increase of the average value for the compressed image. A probable cause for this might be the compression process itself. These errors have to be taken into account for future work carried out using the video recording option.

Table 2: Pixel values for the RAW data and compressed JPEG file for the Nikon 1 V1

Nikon 1 V1 (RAW data) DSC_0621.NEF						
x	1403	1403	1403	1403	1403	1403
y	1340	1345	1366	1382	1424	1441
R values	24	24	22	21	23	24
G values	13	13	11	11	12	13
B values	58	58	56	59	57	58
Nikon 1 V1 DSC_0621.JPEG						
x	1403	1403	1403	1403	1403	1403
y	1340	1345	1366	1382	1424	1441
R values	19	16	17	15	17	17
G values	10	7	10	6	6	8
B values	55	49	51	42	48	53

Recording video films in the right exposure turned out to be more difficult than firstly thought. Using equation 4, several exposure values have been calculated and implemented with a non-satisfactory but overall improved outcome. At the start of the project an exposure of 0.074 was used. This progressed to 0.056, 0.043 and 0.025. Additional neutral density filers were used to improve the outcome but the obtained photos remained slightly saturated.

More work is needed to solve this problem. Following are two examples of recorded impact light flashes.

Figure 49: Impact light flash for shot ID G301112#2

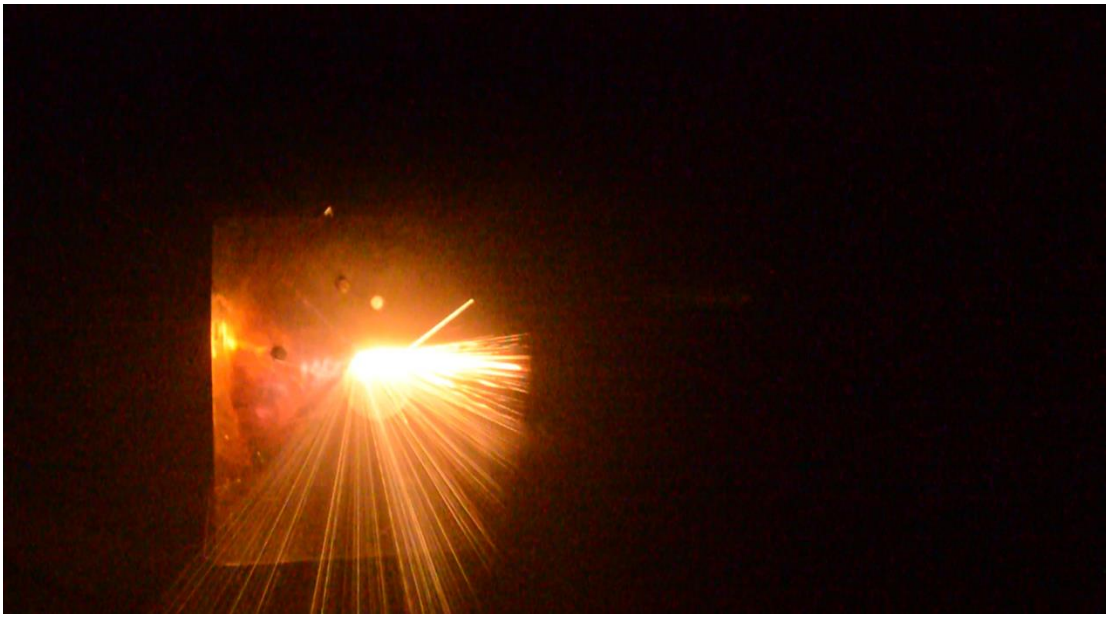

Figure 50: Impact light flash for shot ID G310113#1

Spectral Recordings

Five spectra were recorded of a nylon projectile impacting aluminium plates (Figure 44), one spectrum was recorded for a PTFE projectile impacting on Aluminium plates (Figure 45), and two spectra were recorded for a glass projectile impacting on Aluminium foils (Figure 46). Two spectra of a basalt projectile impacting a basalt target were recorded, but of such poor quality that any interpretation failed. This data was not included here in this discussion. Looking at the plot of the nylon/aluminium impact, one can see that the spectrum exhibits blackbody radiation and atomic line emission. This is in agreement with Friichtenicht [12] and Sugita [29]. Several peaks overlay very nicely, which is expected for the same materials involved. The peaks missing on the lower wavelength range for the lower recorded intensities suggest that the sensitivity of the instrument degrades with lower wavelengths and/or the viewport window is acting as a blocking filter. Taking the shot velocity into account for shot ID G021112#2 and shot ID G231112#2 of 6.32 km^{-1} and 6.65 km^{-1} respectively, one can see that the recorded intensities do not correspond to the fact that a higher velocity has a higher energy. As calculated from the equation for the kinetic energy (E_K in J) of the projectile given as

$$E_K = \frac{1}{2}\, m\, v^2 \qquad \text{Eqn. (9)}$$

where m is the mass (kg) and v the velocity (m s^{-1}) of the projectile and the energy available for the impact was 1517.8 J for shot ID G021112#2 and 1680.5 J for shot ID 231112#2 taken from Table 3.

Table 3: Calculated values of the kinetic energy of the projectiles

	Mass of projectile (kg)	Velocity (m s^{-1})	Energy (J)
G021112#2	7.600×10^{-5}	6320	1517.8
G071112#3	7.600×10^{-5}	6500	1605.5
G231112#2	7.600×10^{-5}	6650	1680.5
G141212#2	1.600×10^{-4}	5500	2420.0
G300113#3	1.600×10^{-4}	5300	2247.2
G231112#3	1.033×10^{-5}	6440	214.2
G301112#2	1.033×10^{-5}	6320	206.3
G300113#1	1.400×10^{-4}	5950	2478.2

This should translate in a higher intensity recorded for the shot ID G231112#2 than for shot ID G021112#2. The reason for this is certainly the pointing accuracy of the spectrometer before impact. Tests carried out with the spectroscope and the fibre optic cable confirmed a very narrow observing angle and a sharp drop of the recorded intensities outside this range. However a blackbody curve fit was made to estimate the impact flash temperature using Wien's displacement law.

$$T = \frac{2.898\, mm\, K}{\lambda_{max}\, nm} \qquad \text{Eqn. (10)}$$

The calculated results are given in Table 4

Table 4: Calculated impact flash temperature form the graphical approximation of a blackbody curve

Shot ID	Wavelength (nm)	Temperature (K)
G021112#2	655±10	4424±69
G071112#3	506±10	5727±69
G231112#2	673±10	4306±69
G141212#2	646±10	4486±69
G300113#1	594±10	4878±69
G300113#3	658±10	4404±69

These calculated temperatures are considerable higher than the previously estimated temperatures, except the PTFE/Aluminium impact. This is explained by the fact that the peak temperature for the materials involved lasted only a very short period of time whereas a 100 milliseconds integration time for the spectroscope was used. This will give the average temperature over the 100 millisecond period. The shift in the peak of the blackbody temperature suggests a velocity dependence of the resultant blackbody curves. To explore this dependence a hypervelocity impact programme can be initiated with the goal of creating numerous blackbody curves. Done this, the peak temperatures should follow a linear relationship for the given materials involved. With this equation of a straight line it would be possible to identify unknown impact velocities for given materials.

Another goal to accomplish was the detection of spectral emission lines in order to identify chemical elements present in the impact plume. The method used worked well and several elements were identified. For the impact of nylon on aluminium (Shot ID G071112#3) ferritin, magnesium, aluminium, nitrogen, carbon, and hydrogen lines were identified. As nylon is a made of oxygen, carbon, nitrogen, and hydrogen atoms and aluminium 6061 alloy is made mainly of aluminium with magnesium and ferritin, the result is not surprising. For the impact of glass on aluminium (Shot ID G30112#2) ferritin, silicon, sodium and calcium lines were detected. This agrees with the composition of the soda-lime glass and the aluminium foil. In the PTFE on aluminium impact (Shot ID G300113#1) ferritin, oxygen, magnesium, carbon and fluorine were identified. Table 5 in the appendix shows the complete list of elements identified for the most pronounced peaks of the spectra recorded.

Conclusion

Measuring the impact flash of hypervelocity impacts can provide important information about the projectile involved as well as other parameters such as impactor velocity. Using consumer graded equipment for these tasks a calibration of the equipment is needed. As this project was set out in the beginning with the aims of measuring the speed of impact by measuring the colour temperature of the impact flash and measuring the impactor size by measuring the impact flash intensity, not all goals have been achieved. The calibration of the cameras Nikon 1 V1 and Nikon D3200 has been achieved and will play a vital role in future impact flash investigations at the hypervelocity impact laboratory. A calibrated helium emission lamp was photographed first. This yielded the equation $\lambda = 2.4704d + 454.63$ nm. Using this equation and the equipment built, it is possible to identify emission lines of an unknown wavelength. However, the self-build spectroscope was not used for impact flash spectroscopy due to delays refining the setup. Instead, a spectroscope on loan from the teaching laboratory was used for this purpose. This was the first time that the hypervelocity impact laboratory recorded spectra of impact flashes. To continue this work the laboratory is currently planning to upgrade a viewport to extent the observable wavelength range as well as securing extra funds for purchasing a new spectroscope. This will enable the hypervelocity impact laboratory to implement a database of impact images and spectra freely accessible for use by the shock physics and hypervelocity impact research communities. Running this project in conjunction with students Mr. Ricky Hibbert and Miss Kathryn Styles meant that most of the hypervelocity impacts produced were of different material composition than Basalt on Basalt. This can be incorporated in possible future work.

Using compressed data formats of the extracted video images, it became necessary to perform an error evaluation for both cameras. This analysis for the Nikon 1 V1 produced a 27 % error in the average pixel value compared to the RAW data for the red pixels, a 36 % error in the pixel value compared to the RAW data for the green pixels, and a 12 % error compared to the RAW data for the blue pixels. The errors calculated for the average pixel value of the Nikon D3200 for the red, green and blue pixels were 16.4%, 42.7%, and -2.7% respectively. This approximation has to be used before any meaningful data is extracted of the compressed data files.

A new target holder was designed by the author to avoid a trip hazard in the hypervelocity impact laboratory. This also allowed the setup of both cameras for impact flash recording. Finally, a poster of this project was presented at the PETER conference at the Institute of Physics (IoP), chaired by the Institute of Shock Physics held in February 2013.

Acknowledgement

The author gratefully acknowledges the assistance of Dr Mark C. Price, Mike J. Cole and Prof Mark J. Burchell for their excellent project supervision. Furthermore I would like to thank Dr Penelope J. Wozniakiewicz together with Andy Morris and Dina Pasini for their support during this project as well as Ricky Hibbert for his help in setting up targets and instrumentation. Finally, I would like to thank Dr Dave M. Pickup along with Dr Victoria Fitzgerald for loaning me some of their technical equipment for my project plus the workshop of the physics department for building my camera holder for the impact chamber.

References

[1] Friichtenicht JF. Investigation of high-speed impact phenomena. Volume 1. National Aeronautics and Space Administration. 1965 Dec. 39 p. Report No.: NASA-CR-70032. [Internet]. [updated 2008 Aug 26; cited 2012 Dec 30].
Available from:
http://ntrs.nasa.gov/archive/nasa/casi.ntrs.nasa.gov/19660007418_1966007418.pdf

[2] Eichhorn G. Measurements of the light flash produced by high velocity particle impact. Planetary and Space Science. 1975; 23: 1519-1525

[3] Eichhorn G. Analysis of the hypervelocity impact process from impact flash measurements. Planetary and Space Science. 1976; 24: 771-781

[4] Eichhorn G. Heating and vaporization during hypervelocity particle impact. Planetary and Space Science. 1977; 26: 463-467

[5] Burchell MJ, Cole MJ, Ratcliff PR. Light flash and Ionization from hypervelocity Impacts on Ice. Icarus.1996; 122: 359-365

[6] Madiedo JM, Ortiz JL, Morales N, Cabrera J. Monitoring and analysis of flashes produced by meteoroids impacting on the lunar surface. EPSC Abstracts. 2012; 7: EPSC2012-59 2012

[7] Margonis A, Sohl F, Flohrer J, Christou A, Oberst J. Telescopic Ground Observations for Lunar Impact Flash Detection using the SPOSH camera. EPSC Abstracts. 2012; 7: EPSC2012-562 2012

[8] National Aeronautics and Space Administration. Voyages: Charting the Course for Sustainable Human Space Exploration. Langley Research Center. [Internet]. 2012 [Cited 2013 Jan 22].
Available from:
http://www.nasa.gov/pdf/657307main_Exploration%20Report_508_6-4-12.pdf

[9] Graham RA. Solids under high-pressure shock compression. New York: Springer Verlag New York, Inc.; 1993.

[10] Meyers MA. Dynamic behaviour of materials. New York: John Wiley & Sons, Inc.; 1994

[11] Burchell MJ, Cole MJ, McDonnell JAM, Zarnecki JC. Hypervelocity impact Studies using the 2 MV Van de Graaff accelerator and two-stage light gas gun of the University of Kent at Canterbury. Measurement Science and Technology. 1999; 10 (1): 41-50

[12] Friichtenicht JF. Investigation of high-speed impact phenomena. Volume 2. National Aeronautics and Space Administration. 1965 Dec 1. 231 p. Report No.: NASA-CR-69894. [Internet]. [updated 2011 Apr 7; cited 2012 Dec 30].
Available from:
http://ntrs.nasa.gov/archive/nasa/casi.ntrs.nasa.gov/19660006916_1966006916.pdf

[13] Lee N, Close S, Lauben D, Linscott I, Goel A, Johnson T et al. Measurements of freely – expanding plasma from hypervelocity impacts. Stanford University. [Internet] 2011 [cited 2013 Feb 24].
Available from:
http://sess.stanford.edu/sites/default/files/pubs/jrnl/201201%20-%20IJIE%20-%20Lee%20-%20RPA%20-%20Preprint.pdf

[14] Froebrich D. Colour CCD's [unpublished lecture notes]. PH507: The Multiwavelength Universe and Exoplanets, University of Kent; lecture given 2011

[15] Tipler PA, Mosca G. Physics with modern Physics for Scientists and Engineers. 6th ed. New York: W.H. Freeman and Company; 2008.

[16] Froebrich D. Complex atoms [unpublished lecture notes]. PH503: Atomic and Nuclear Physics, University of Kent; lecture given 2011

[17] Sadler PM. Projecting Spectra for Classroom Investigations. The Physics Teacher. 29(7). 1991. Pp. 423-427

[18] Some printable paper rulers [Internet] 2002 [updated 2002 Sep 7; cited 2013 Jan 21].
Available from:
http://www.vendian.org/mncharity/dir3/paper_rulers/UnstableURL/meterstick_large.pdf

[19] VideoPad video editor software [Internet] 2012 [cited 2012 Nov 13]
Available from:
http://www.nchsoftware.com/videopad/de/index.html

[20] Kramida A, Ralchenko Y, Reader J, and NIST ASD Team (2012). NIST Atomic Spectra Database (ver. 5.0), [Online]. [updated 2013 Feb 28; cited 2013 Mar 4] National Institute of Standards and Technology, Gaithersburg, MD
Available from
http://physics.nist.gov/asd

[21] Melosh HJ. Impact cratering – A geologic process. New York: Oxford University Press.; 1989

[22] Marsh SP. LASL shock Hugoniot data. Los Angeles: University of California Press.; 1980; 674p

[23] Wozniakiewicz PJ, Ishii HA, Kearsley AT et al. Investigation of iron sulphide impact crater residues: A combined analysis by scanning and transmission electron microscopy. Meteoritics & Planetary Science. 2011; 46 (7): 1007-1024

[24] Artemieva N. and Ivanov B. Launch of Martian meteorites in oblique impacts. Icarus. 2004; 171: 84-101

[25] Fritz J, Artemieva N, Greshake A. Ejection of Martian meteorites. Meteoritics & Planetary Science. 2005; 40: 1393-1411

[26] ASM Aerospace Specification Metals Inc. [Internet] 2012 [cited 2013 Mar 4]
Available from:
http://asm.matweb.com/search/SpecificMaterial.asp?bassnum=MA6061t6

[27] Kaye and Laby "Modern Plastics Encyclopedia", 1971, McGraw-Hill Inc. New York.

[28] Yutopian Online. [Internet] 2000 [cited 2013 Mar 4] Available from: http://www.yutopian.com/Yuan/prop/Teflon.html

[29] Sugita S and Schultz P. Spectroscopic measurements of vapour clouds due to oblique impacts. Journal of Geophysical research. 1998; 103 (E8): 19427-19441

[30] MDC Vacuum Limited. [Internet]. 2013 [cited Mar 4] Available from : http://www.mdcvacuum.co.uk/en/catalogue/index.htm?xpath=/section%5B5%5D

Image Credits

Cover-page	Arms of the University of Kent (Wikipedia) [image on the internet]. 2011 [updated 2012 Oct 14; cited 2013 Jan 7]. Available from: http://www.google.de/imgres?q=arms+of+the+university+of+kent+png&hl=de&sa=X&biw=944&bih=1061&tbm=isch&tbnid=fh-1RjfF2lYnyM:&imgrefurl=http://en.wikipedia.org/wiki/File:Arms_of_the_University_of_Kent.png&docid=kjC1JcxBZlaMAM&imgurl=http://upload.wikimedia.org/wikipedia/en/5/5e/Arms_of_the_University_of_Kent.png&w=310&h=262&ei=dNopUe3AN-Wc0QW41oG4CQ&zoom=1&iact=hc&vpx=4&vpy=102&dur=6417&hovh=206&hovw=244&tx=79&ty=118&sig=117570723207162731896&page=1&tbnh=135&tbnw=160&start=0&ndsp=39&ved=1t:429,i:82
Figure 6	Nikon D3200 (Digital Camera resource page) [image on the internet]. 2012 [updated 2012 Nov 13; cited 2013 Jan 30]. Available from: http://www.google.de/imgres?q=image+Nikon+D3200&hl=de&sa=X&biw=944&bih=1061&tbm=isch&tbnid=QifiqONKrMPuBM:&imgrefurl=http://www.dcresource.com/reviews/nikon/d3200-review&docid=src_t0TOye0BIM&imgurl=http://www.dcresource.com/sites/default/files/imagecache/gallery_large/reviews/nikon-d3200/camera-front-angled.jpg&w=500&h=500&ei=MN0pUb7POYnb0QWIyYCgBA&zoom=1&iact=hc&vpx=510&vpy=667&dur=290&hovh=225&hovw=225&tx=153&ty=81&sig=117570723207162731896&page=1&tbnh=149&tbnw=155&start=0&ndsp=30&ved=1t:429,i:172
Figure 7	Nikon 1 V1 (picspack) [image on the internet]. 2011 [updated 2011 Sept 26; cited 2013 Jan 30]. Available from: http://www.picspack.de/blog/wp-content/uploads/2011/09/Nikon_1_V1_1_Nikkor_VR_30-110_WH.jpg
Figure 14	Spectrum tube power supply (fisher scientific) [image on the internet]. 2009 [cited 2013 Feb 26]. Available from: http://www.google.de/imgres?q=spectrum+tube+power+supply&hl=de&sa=X&biw=1920&bih=1077&tbm=isch&tbnid=NKQyydCBWDyP0M:&imgrefurl=https://www.fishersci.ca/browseResults.do%3Fcid%3D2643856&docid=AdekRDuYqgY1DM&imgurl=https://www.fishersci.ca/images/F59817~wl.jpg&w=237&h=460&ei=NM0sUafqJsKy0QWBlICYAw&zoom=1&iact=rc&dur=517&sig=117570723207162731896&page=1&tbnh=132&tbnw=78&start=0&ndsp=73&ved=1t:429,r

:56,s:0,i:256&tx=28&ty=74

Figure 15 Emission tube (Science first) [image on the internet]. 2013 [cited 2013 Feb 26]. Available from: http://www.sciencefirst.com/Spectrum-Tube-Helium.html

Figure 16 Diffraction grating (rapid online) [image on the internet]. 2012 [cited 2013 Feb 26]. Available from: http://www.rapidonline.com/catalogueimages/module/M500147P01WL.jpg

Figure 17 CD Spectroscope (mindsetsonline) [image on the internet]. 2013 [cited 2013 Jan 31]. Available from: http://www.mindsetsonline.co.uk/product_info.php?cPath=18_622_606&products_id=1009497

Figure 18 Spectroscope (science first) [image on the internet]. 2013 [cited 2013 Jan 31]. Available from: http://www.sciencefirst.com/Spectroscope-Set-15.html

Figure 28 USB650 Red Tide Spectrometer with optical fibre (Ocean Optics) [image on the internet]. 2012 [cited 2013 Jan 30]. Available from: http://www.oceanoptics.com/Products/usb650.asp

Table 5: Identified elements in spectra using the NIST website

Nylon projectile impacting Aluminium plates		
peak at wavelength	Ion	Measured wavelength in nm from NIST
peak (309 nm)	Fe I	309.02046
peak (358 nm)	Fe I	358.11928
peak (383 nm)	Fe I	383.07572
peak (398 nm)	Fe I	398.17708
peak (438 nm)	Mg I	438.0375
peak (448 nm)	Fe I	448.01363; 448.0271
peak (466 nm)	Fe I	466.0431
	Al II	466.3056
peak (487 nm)	Fe I	487.13178
peak (519 nm)	Fe I	519.14546
peak (559 nm)	Al II	559.3302
peak (571 nm)	N II	571.077
peak (589 nm)	C II	588.977; 589.159
peak (624 nm)	Fe I	624.0310; 624.06458
peak (656 nm)	H I	656.2709699
peak (706 nm)	Mg I	706.0409
	Al II	705.660
Glass projectile impacting Aluminium foils		
peak at wavelength	Ion	Measured wavelength in nm from NIST
peak (396 nm)	Fe I	396.02789

peak (569 nm)	Si I	569.04967
	Fe I	569.14967
peak (589 nm)	Na I	588.9950954
peak (616 nm)	Fe I	615.93730
	Ca I	616.129
PTFE projectile impacting Aluminium plate		
peak at wavelength	Ion	Measured wavelength in nm from NIST
peak (309 nm)	Fe I	309.02046
peak (396 nm)	Fe I	396.02789
peak (469 nm)	Fe I	469.0138
peak (516 nm)	Fe I	515.90573
peak (558 nm)	O I	557.734
peak (571 nm)	Mg I	571.10880
peak (589 nm)	C II	588.997
peak (755 nm)	F I	755.224